Analysis of the M_w 7.5 25th February 2018 Papua New Guinea earthquake using the sub-pixel offset method

Jeng Hann Chong

25th April 2019

Dr. Mong-Han Huang

GEOL 394

Abstract
Papua New Guinea is situated at the margin between the Pacific and Australian Plates, a boundary with a rapid total convergence rate of ~110 mm/yr. Papua New Guinea is in a complex geological setting due to the high convergence rate and the oblique collision between the Australian Plate and Pacific Plate. On 25th February 2018, an M_w 7.5 earthquake struck the Southern Highlands in the Papuan Fold and Thrust Belt. According to the United States Geological Survey, the mainshock was followed by more than 260 M 4+ aftershocks around the Southern Highlands within a month. Fault slip models produced by the USGS using teleseismic stations (>1000 km away from the hypocenter) estimated the fault associated with the mainshock is 210 km in length and 60 km width. The strike of the fault is 308° with a dip of 35°. The depth of the mainshock is estimated to be at 15 km. However, the fault geometry and the hypocenter of the mainshock are not well-constrained due to the absence of land-based geodetic systems such as Global Positioning Systems and the lack of a dense seismic network around the Papuan Fold and Thrust Belt. The goal of my research is to understand the fault structure involved in the earthquake. The method used is a satellite geodetic method known as the sub-pixel offset of Synthetic Aperture Radar (SAR) images that can be utilized to provide information about the 3D coseismic (during the earthquake) surface displacement.

I've identified two prominent surface ruptures from two different faults (Mubi Fault and Mananda Fault) involved in this mainshock. Mubi Fault is located closer to the hinterland in the Imbricate Belt and Mananda Fault is located at the Strongly Folded Belt, the frontal part of the fold-and-thrust belt. Both faults have an NW-SE structure aligning with the general trend of Papuan Fold and Thrust Belt. Mubi Fault has an estimated surface rupture length of ~35 km with a peak vertical uplift of ~2.1 meters and ~2 meters of southward displacement. Whereas, Mubi Fault has an estimated surface rupture of ~22 km long with ~1.1 meters of peak vertical uplift and ~3 meters of southward displacement. The dip angle of the modeled Mubi Fault is 35° and 15° for the Mananda Fault. A detachment fault with a length of 130 km was used to explain the discontinuity between the two surface rupturing faults located at different parts of the fold-and-thrust belt. The sub-horizontal detachment fault has a dip of 6°. The peak slip is ~6.04 meters and is located in Mubi Fault. The mainshock calculated was a M_w 7.24. The sub-pixel offset method presents a method that is capable of understanding fault structures involved in earthquakes using surface displacement in densely forested regions and that it can be used by first responders to quickly analyze and prioritize their rescue efforts.

Content

1. Introduction ---------- 3

2. Background

    2.1 Tectonic setting of Papua New Guinea ---------- 3

    2.2 Structure of the Papuan Fold and Thrust Belt ---------- 4

    2.3 Tectonic movement of the Papuan Fold and Thrust Belt ---------- 6

    2.4 Seismicity in the Southern Highlands ---------- 6

3. Objective ---------- 8

4. Hypotheses ---------- 10

5. Significance ---------- 10

6. Methods

    6.1 Sub-pixel offset ---------- 10

    6.2 Fault slip model ---------- 13

7. Results

    7.1 Surface displacement ---------- 14

    7.2 Identification and removal of landslides ---------- 18

    7.3 Fault slip model ---------- 19

8. Uncertainty ---------- 22

9. Discussion ---------- 23

10. Broader Impacts ---------- 28

11. Summary ---------- 29

12. Bibliography ---------- 30

13. Appendix ---------- 33

1. Introduction

On the 25th of February 2018, an M_w 7.5 earthquake struck the Southern Highlands in the Papuan Fold and Thrust Belt. According to the United States Geological Survey earthquake catalog, the mainshock was followed with more than 260 aftershocks of M 4+ over the span a month. The mainshock on the 25th February 2018 was the largest magnitude earthquake that has been recorded in the Southern Highlands using the seismic moment magnitude scale (Ghasemi et al., 2016). A finite fault solution from the USGS produced using teleseismic stations estimated that the epicenter of the mainshock to be located behind the frontal part of the Papuan Fold and Thrust Belt with the mainshock located a depth of approximately 15 km. The fault solution included an expectation of the fault area of 85 km by 30 km with a strike of 308°, dipping in a northeast direction at 35°, and a rake of 77°.

The goal of this research is to define the fault structure in the Papuan Fold and Thrust Belt using satellite geodetic measurements. The satellite geodetic method applied is known as the sub-pixel offset and it used to determine the 3D coseismic surface displacement of the mainshock. The coseismic surface displacement is also used to identify surface ruptures and to estimate the faults involved in the earthquake. The surface displacements from the sub-pixel offset method are jointly used in the fault slip model. Fault slip model presents a way to estimate the size, the slip distribution and the fault parameters of the faults involved in this mainshock.

2. Background

2.1. Tectonic Setting of Papua New Guinea

The northern margin of Papua New Guinea is bounded by two active subduction zones, namely the New Britain Trench and the New Guinea Trench along the eastern side towards Indonesia (Ripper and McCue, 1983; Heidarzadeh et al., 2015) (Figure 1). Large magnitude earthquakes related to the active subduction along the northern margin of Papua New Guinea is also known to generate tsunamis such as the one 1999 that was initiated by a M_s 7.1 earthquake (Koulali et al., 2015; Satake and Tanioka, 2003). The northern region of Papua New Guinea comprises accreted arcs known as Finisterre Arcs (FA). The Finisterre Arcs is bounded by the Ramu-Markham Fault (RMF). The Ramu-Markham Fault is the result of oblique convergence between the Melanesian arc and New Guinea (Baldwin et al., 2012), and experiences a greater slip in the west than in the east. The Mobile Belt (MO), south of the Ramu-Markham Fault is a series of strike-slip faults across the New Guinea that were activated in the Late Pliocene. The New Guinea Highlands (NGH) located at the center of Papua New Guinea and it stretches all along the length of the island. The New Guinea Highlands formed from a 15 km inverted slab trusted to the surface (Hill et al., 2003). The New Guinea Highlands started rising from below sea level ~12 Mya (Baldwin et al., 2012). To the south of the New Guinea Highlands lies a stable platform that is a part of the Australian Continent. The stable platform is considered as an aseismic platform with an estimated elevation of <100 meters (Baldwin et al., 2012). In between the stable platform and the New Guinea Highlands is the Papuan Fold and Thrust Belt. The suture zone between the Papuan Fold and Thrust Belt and the accreted arc north of Papua New Guinea is marked by ophiolites and high pressure and temperature metamorphic rocks (Baldwin et al., 2012). Foreland basin structures only existed in the western part of the New Guinea Island, mainly in Indonesia. The lack of foreland basins in Papua New Guinea is due to a weaker continental crust (Hill et al., 2003).

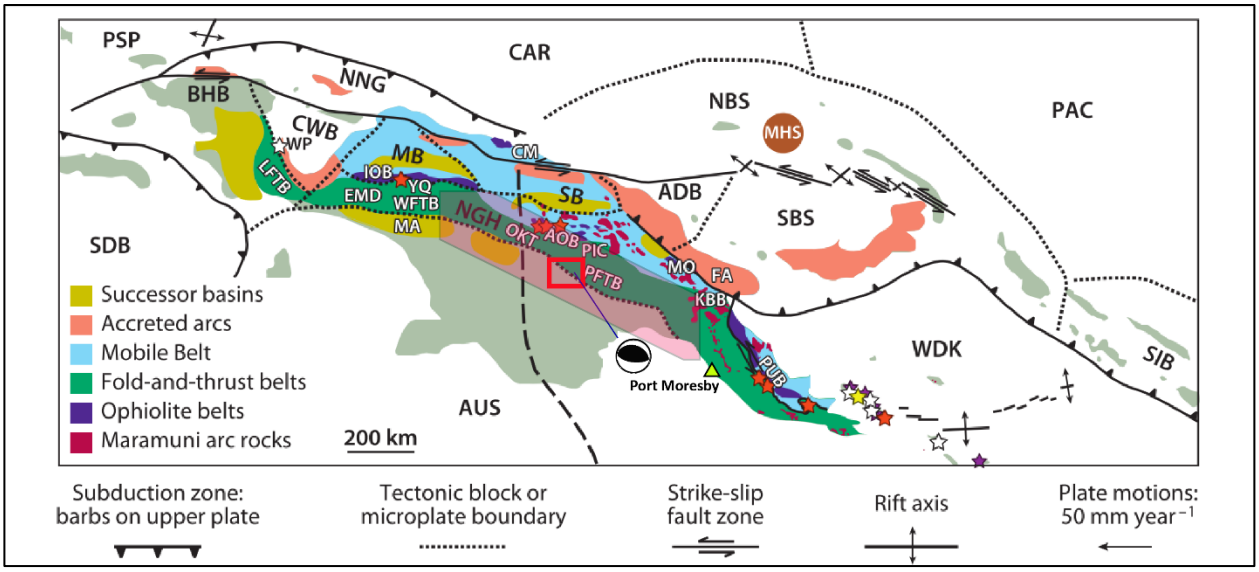

Figure 1: Geological map of New Guinea. The area of study around the mainshock is indicated with a red box (Figure 2). The lime-green triangle indicates the capital of Papua New Guinea, Port Moresby. PFTB stands for Papuan Fold and Thrust Belt. The red highlighted area is the Southern Highlands (Ripper and McCue, 1983). Oblique convergence between the Pacific Plate (PAC) and Australian Plate (AUS) during the Miocene to Pliocene triggered the formation of microplates. Abbreviations: ADB, Adelbert block; AOB, April ultramafics; BHB, Bird's Head block; CM, Cyclops Mountains; CWB, Cendrawasih block; CAR, Caroline microplate; EMD, Ertsberg Mining District; FA, Finisterre arc; IOB, Irian ophiolite belt; KBB, Kubor & Bena blocks; LFTB, Lengguru fold-and-thrust belt; MA, Mapenduma anticline; MB, Mamberamo Basin block; MO, Marum ophiolite belt; MHS, Manus hotspot; NBS, North Bismarck plate; NGH, New Guinea highlands block; NNG, Northern New Guinea block; OKT, Ok Tedi mining district; PSP, Philippine Sea plate; PUB, Papuan Ultramafic Belt ophiolite; SB, Sepik Basin block; SDB, Sunda block; SBS, South Bismarck plate; SIB, Solomon Islands block; WP, Wandamen peninsula; WDK, Woodlark microplate; YQ, Yeleme quarries. Figure modified from Baldwin et al. (2012).

2.2. Structure of the Papuan Fold and Thrust Belt

The Southern Highlands is an area of 700 km long and 100 km wide that stretches from the Gulf of Papua to the border of Indonesia and Papua New Guinea (Ripper and McCue, 1983). The Southern Highlands is also considered to be the boundary between the Australian and Highlands block (Koulali et al., 2015). A study by Hill et al. (2010) divided the Papuan Fold and Thrust Belt into four sections (Figure 2): 1) Gently Folded Belt 2) Strongly Folded Belt 3) Imbricate Belt; and, 4) Distal Facies. The Gently Folded Belt is the southernmost end of the fold-and-thrust belt which is adjacent to the Darai Plateau and it has the least degree of folding (Figure 3). The Strongly Folded Belt is an important source for oil and gas (Davies, 2012). Detachment-involved thrusting is also expected at the Strongly Folded Belt and Imbricate Belt (Abers and McCaffrey, 1988). North of the Strongly Folded Belt is the Imbricate Belt that starts from Lake Kutubu and ends at the Wage Anticline that consists of Miocene limestone and upper Cretaceous shales. Out-of-sequence thrust faults are thought to exist in the Imbricate Belt. Hill et al., (2010) proposed that out-of-sequence and backthrust earthquakes in the Imbricate Belt were caused by the lack of space for an active displacement adjacent to the foreland.

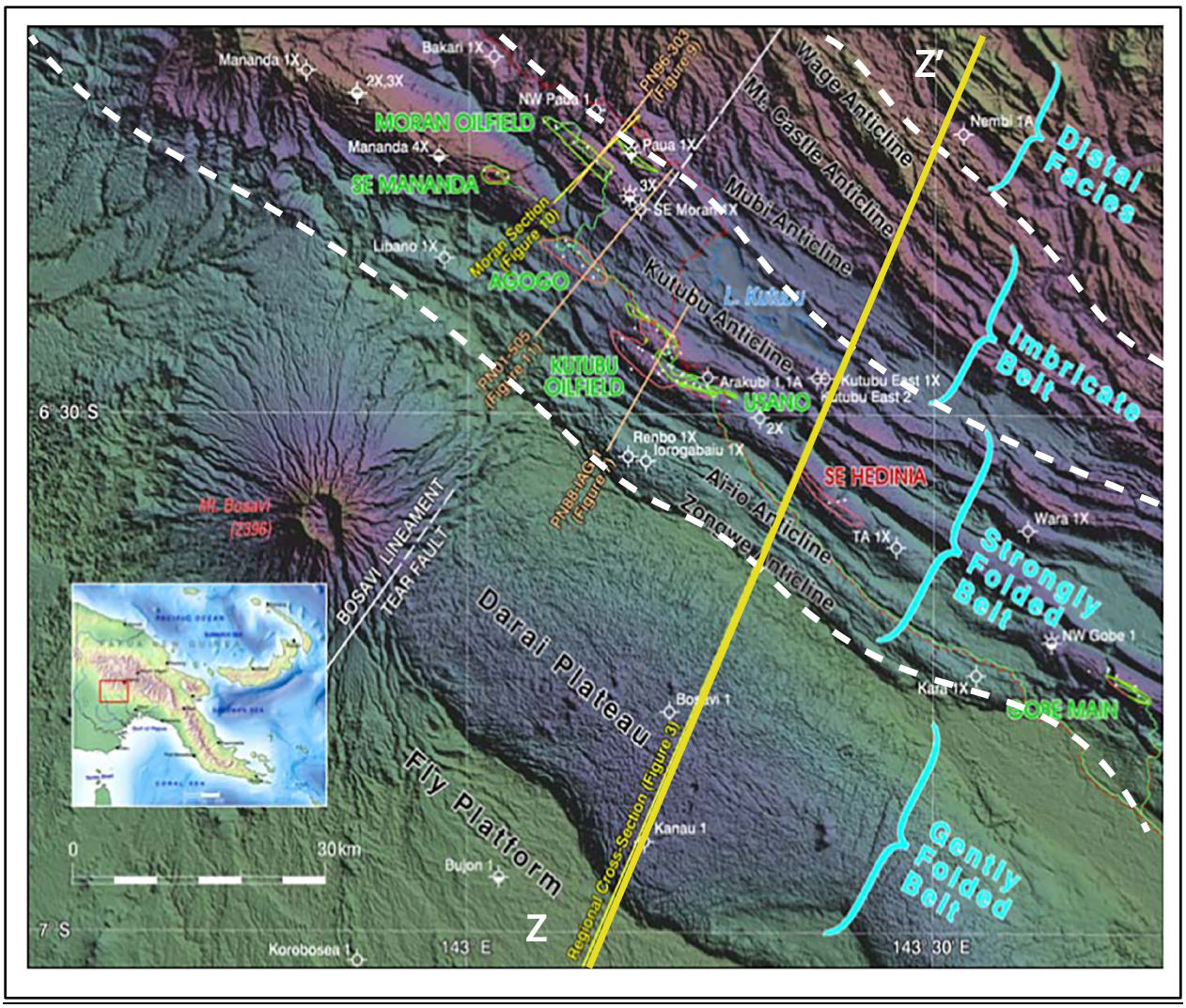

Figure 2: Topographic map of the Southern Highlands in the Papuan Fold and Thrust Belt. The extinct volcano, Mount Bosavi is pictured on the left-center. Figure modified from Hill et al., (2010). The hypocenter of the mainshock constrained by USGS is out of frame in this figure. The yellow line highlights the cross-section across the Papuan Fold and Thrust Belt shown in Figure 3.

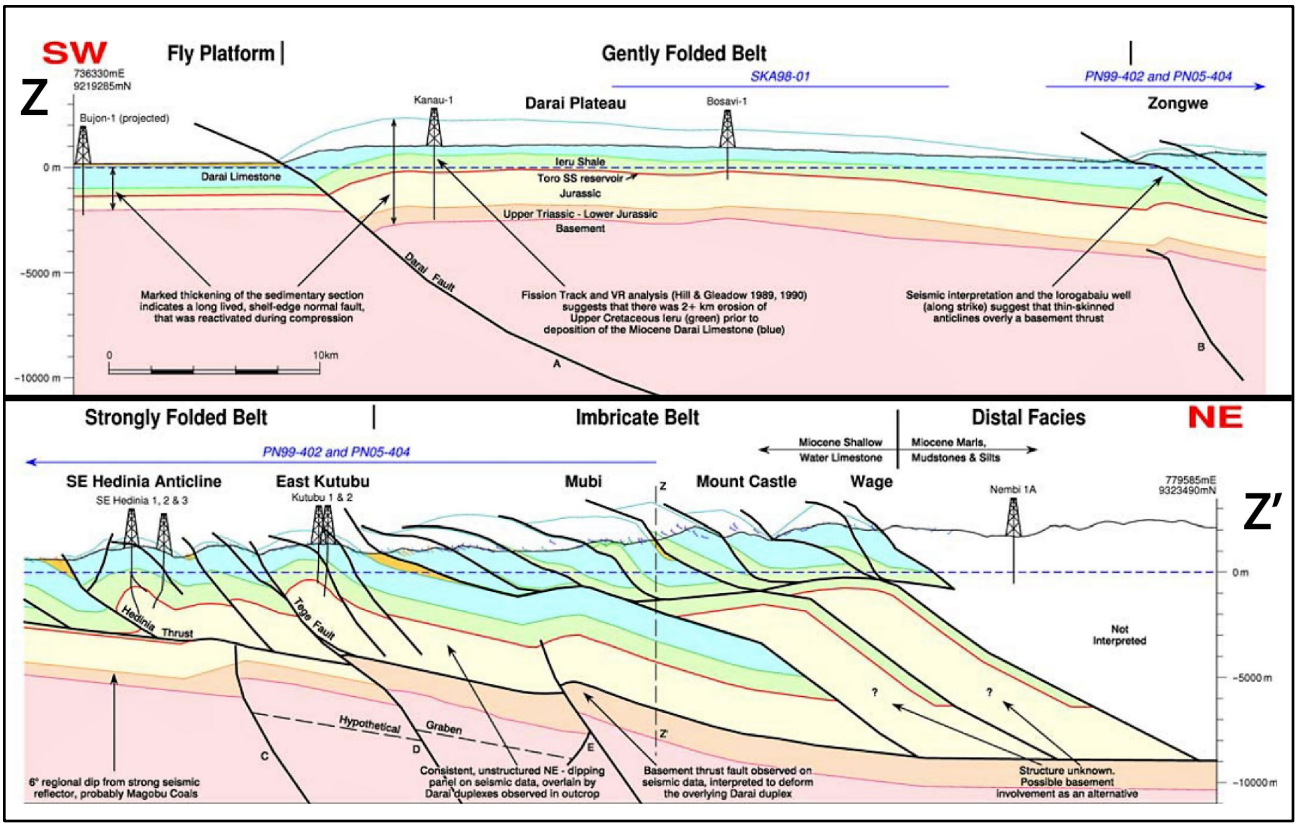

Figure 3: Cross-section of the Southern Highlands. Most of the oil and gas extraction takes place in the Strongly Folded Belt. The Strongly Folded Belt starts from Zongwe on the top figure and ends around the East Kutubu. Figure from Hill et al., (2010).

2.3. Tectonic movement of the Papuan Fold and Thrust Belt

The relative convergence rate between the Australian Plate and the Pacific Plate is ~110 mm/yr with an azimuth of 70° relative to the Pacific Plate (Tregoning et al., 2000; Wallace et al., 2004). It is estimated that the convergence experienced in New Guinea is ~70 mm/yr (Tregoning and Gorbatov, 2004). The convergence across New Guinea is accommodated by the Papuan Fold and Thrust Belt and New Guinea Trench. The Papuan Fold and Thrust Belt accommodates about 5% - 20% of the convergence. Whereas, the remaining convergence is accommodated by the New Guinea Trench (Abers and McCaffrey, 1988). Koulali et al. (2015) also proposed that the New Guinea Highlands is rotating clockwise. The convergence rate decreases from 12 ± 0.7 mm/yr along the eastern side to 6.8 ± 0.7 mm/yr to the western side. The Southern Highlands experiences a convergence rate of ~6 to 13 mm/yr between the Australian Plate and the New Guinea Highlands and changing to a strike-slip motion towards the west.

2.4. Seismicity in the Southern Highlands

Prior to 25th February 2018, there were three large-magnitude earthquakes that were recorded in the Southern Highlands. An M_w 6.2 occurred in 1993 in Hides, a M_w 6.6 in 2000 in Gobe, and a M7.5 that occurred near Kikori in 1922 (Ripper and McCue, 1983; Ghasani et al., 2016). USGS reported that the 25th February 2018 M_w 7.5 mainshock was a thrust fault with a strike of 308°, dipping in a northeast direction at 35°, and with a rake of 77°. The hypocenter is located at 6.070°S 142.754°E (Figure 9) in the Strongly Folded Belt with a seismic moment of 2.192e+20 N-m, equivalent to a M_w

7.49 earthquake. The estimated peak slip of the fault slip model is ~2.3 m at a depth of ~25 km (Figure 5). Within the span of a month after the mainshock, there were at least 260 recorded earthquakes of M_w 4.0+ with the largest aftershock magnitude recorded at M_w 6.7. The USGS earthquake catalog recorded 39 aftershocks occurred within 24 hours after the mainshock (Figure 4).

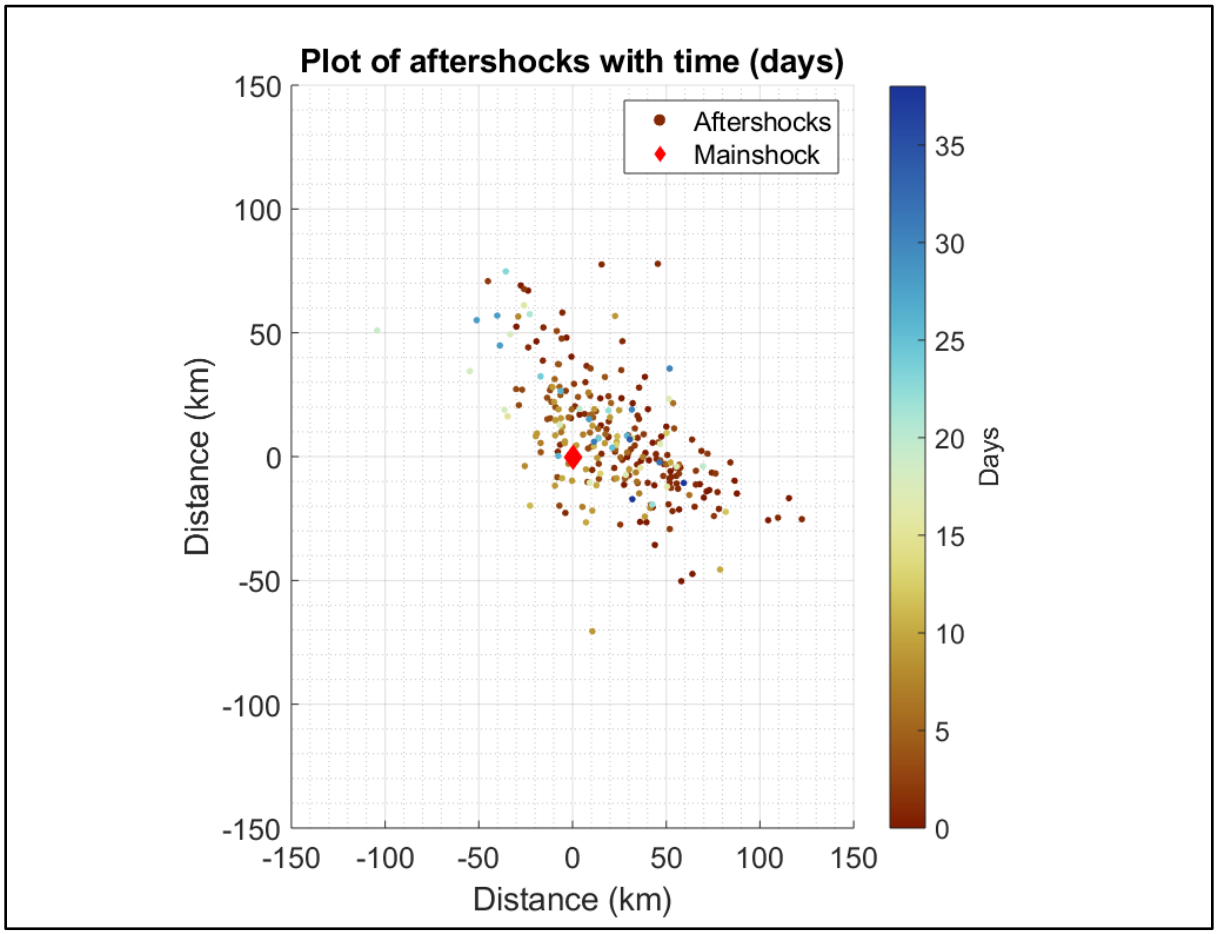

Figure 4: Plot of aftershocks color-coded as a function of time (in days) since the main quake. The distance (km) of the aftershocks from the mainshock at (0,0) km. Warmer colors indicate an increasing duration after the mainshock. The trend of the aftershocks followed the geometry of the Papuan Fold and Thrust Belt.

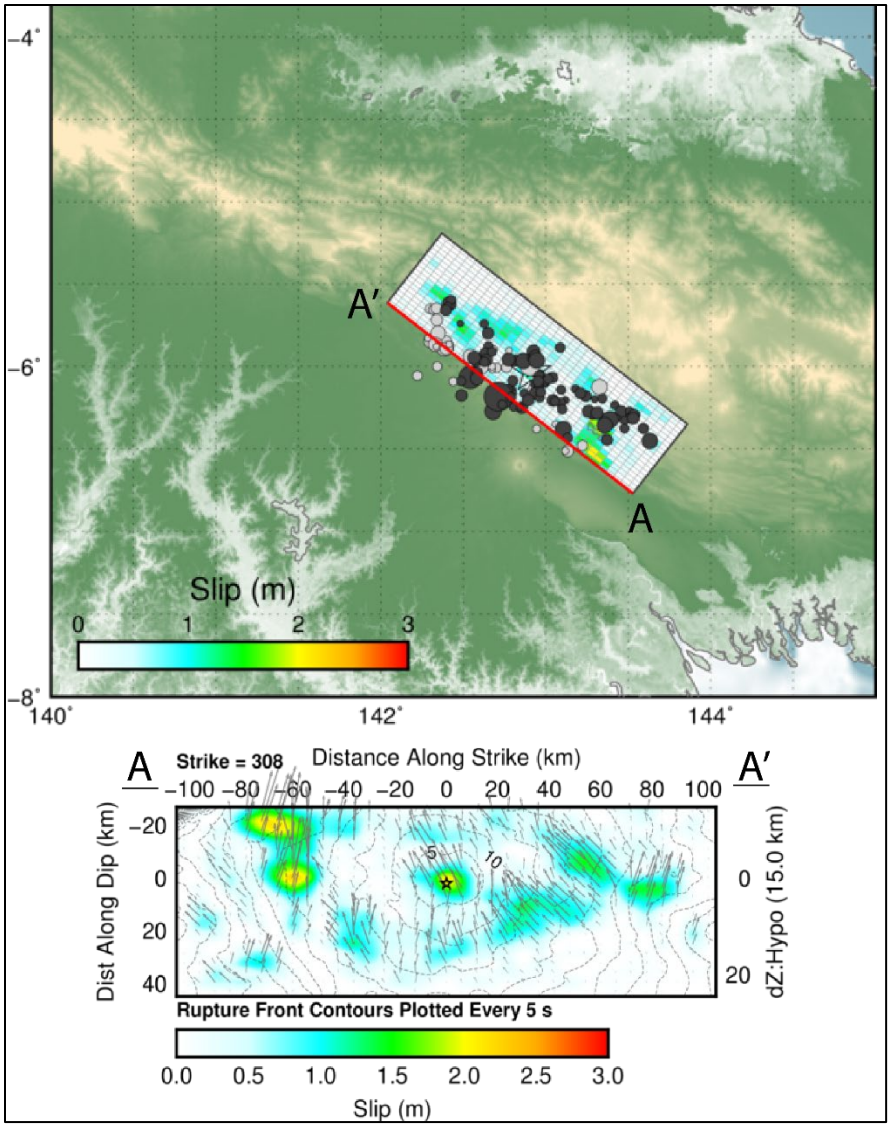

Figure 5: The fault slip model of the USGS was produced using teleseismic data constraints. The fault is 210 km in length and 60 km width. The peak slip is ~2.3 meters at 0 km (distance along dip), -60 km (along strike). Grey circles indicate aftershocks and black circles indicate previous earthquakes.

3. Objectives

Papua New Guinea is one of the most tectonically active regions in the world. Ripper and McCue (1983) estimated the earthquake return period (recurrence interval) for an M 6.9 earthquake is 30 years within the Southern Highlands. They also estimated that large magnitude earthquakes in this region will experience a shaking intensity of 7 out of a scale of 10 within an 80 km radius around the hypocenter. Although the 25th February 2018 mainshock had a large magnitude (M_w 7.5), the location and depth of the mainshock is not well constrained by different agencies that characterize and monitor earthquake activity (Table 1). The distance between the two furthest epicenters is ~35 km (Figure 6).

There are two known seismic stations that are operational in Papua New Guinea. The closest known seismic station is located in Port Moresby the capital of Papua New Guinea, 610 km southeast of the hypocenter (Anton and Gibson, 2015). The USGS earthquake catalog does not have data information for aftershocks with M_w less than 4.0 due to the lack of a dense (appropriate) network of seismic stations within Papua New Guinea. Furthermore, the Papuan Fold and Thrust Belt do not have any land-based geodetic stations such as Global Positioning System (GPS) to measure the coseismic surface displacement precisely. The lack of a dense seismic network and limited GPS stations poses a challenge to precisely constrain the fault geometry and slip distribution. Furthermore, surface ruptures are difficult to map due to the lack of accessibility and the dense vegetation cover (Ripper and McCue, 1983; Abers and McCaffrey, 1988; Hill et al., 2010).

It is also important for existing buildings to be reinforced with the hope of withstanding large magnitude earthquakes within the Papuan Fold and Thrust Belt. Oil and gas companies within the Papuan Fold and Thrust Belt should reinforce their buildings and other structures to prevent catastrophic environmental disasters.

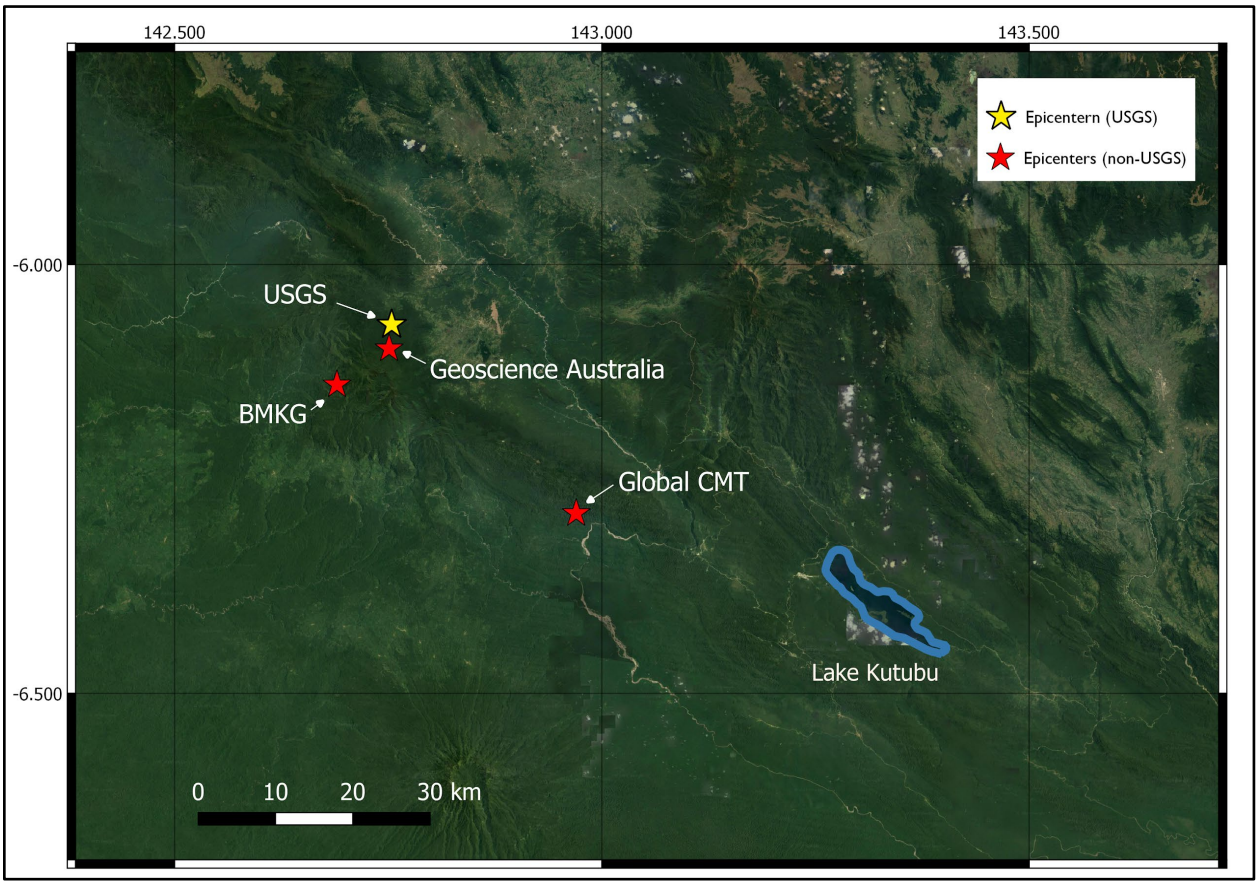

Figure 6: The locations of the mainshock constrained by USGS (yellow), Global CMT, Geoscience Australia, and BMKG. The largest differences in distances are between USGS and Global CMT, with ~35km. The satellite image was obtained from Google Satellite.

Source\Properties	Global CMT	USGS	Geoscience Australia	BMKG (Indonesia)
Depth (km)	12	15	17	32
Latitude & Longitude	-6.29, 142.97	-6.070, 142.754	-6.098, 142.751	-6.14,142.69

Table 1: The characteristics of the 25th February 2018 mainshock in Papua New Guinea as recorded by GlobalCMT (GCMT), USGS, Geoscience Australia, and Indonesian Agency for Meteorology, Climate, and Geoscience (BMKG).

4. Hypothesis

The sub-pixel offset method can provide surface displacements in heavily vegetated areas and in areas with a limited geodetic and seismic network. I hypothesize that there are at least two fault segments that were involved in the mainshock.

5. Significance

I expect that my research will show the importance of using satellite geodetic methods to understand surface deformation caused by an earthquake in areas with dense vegetation. Satellite geodesy methods have improved significantly in recent years with the release of higher resolution Synthetic Aperture Radar (SAR) images. Furthermore, satellite geodesy can also be used to study interseismic slip and slip slow events such as along the Hayward Fault in California (Bürgmann, 2018). The sub-pixel offset method can also be used to analyze large surface movements such as landslides, glacial movement and land deformation due to water pumping in densely forested areas or urban areas (Zhou et al., 2009).

The sub-pixel offset method also provides an alternative for rescue operations to perform a quick damage assessment over a large region. Rescue teams can use the surface displacement map to determine routes that were blocked by earthquake-triggered landslides or destroyed by surface ruptures. Furthermore, results from a previous GPS campaign in the Papuan Fold-and-Thrust Belt demonstrated inconsistencies with expected plate motion that is believed to be caused by landslides (Koulali et al., 2015).

6. Methods

6.1. Sub-pixel offset

Synthetic Aperture Radar (SAR) images were used to perform the sub-pixel offset. SAR is an imaging technique that uses microwave frequency and is therefore not affected by weather and clouds (Burgmann et al., 2000). The source of the radar could be either a plane or satellite. This research uses a satellite operated by the European Space Agency called Sentinel-1. Sentinel-1 uses a short wavelength microwave (C-band) to produce SAR images. The satellite passes a location along two different tracks. As it passes over a location from northeast to southwest, it is known as a descending track and from southeast to the northwest is known as an ascending track (Figure 7). The interval for the satellite to pass over the same location along the same track is 12 days (Haghighi and Motagh, 2017).

The sub-pixel offset method uses two SAR images that were taken before and after the mainshock over the same region to determine the changes of a specific area. The offset is calculated using the normalization cross-correlation of pixels within a fixed bounding box (Cai et al., 2017). Each type of processed track consists of displacement in two directions such as azimuth and range. Azimuth is parallel to the direction of satellite trajectory and range is the line-of-sight that is perpendicular to the direction of the satellite trajectory (Michele et al., 2010). Each pixel of the SAR image covers a

distance of ~5 meters in the range direction and ~20 meters in the azimuth direction (Haghighi and Motagh, 2017). Each ascending and descending track only present displacement information in the line-of-sight relative to the satellite (Bürgmann et al., 2000). A combined image of a descending and an ascending track will be able to provide a 3D surface displacement with components of vertical, north-south, and east-west (Michele et al., 2010). The sub-pixel offset method is also capable of providing near-field surface displacement of >1 meter (Huang et al., 2017).

Tracks A9 (ascending) and D133 (descending) were selected to provide coverage over the region of the mainshock. Each track consists of a pre-earthquake image (master) and a post-earthquake image (slave) (Figure 8). The master and slave images were chosen closest to the date of the mainshock to reduce the effects from other sources (Table 2). A program developed by Jet Propulsion Laboratory (JPL) called the InSAR Scientific Computing Environment (ISCE) was used to process the sub-pixel offsets (Rosen et al., 2012). A correlation pixel window of 64 x 64 pixels with a sliding interval at every 32 pixels in the range direction and 16 pixels in the azimuth direction was used. Preliminary results showed that A9 only covers ⅔ of the surface displacement over the region of interest. Another ascending track listed as A82 was used to provide the remaining ⅓ of the region. The D133 track has coverage over the entire region of interest. The combined pairs of ascending track and descending track are listed as A9-D133 and A82-D133.

The surface displacements of the combined pairs were computed using MATLAB scripts that were provided by Dr. Mong-Han Huang. A median filter was used to provide smoother surface displacement and it can reduce the influence of noise from other sources such as landslides (Dominguez et al., 2003). Median filter calculates the median value of the pixels within a bounding box and replaces the value of the pixel in the center with the median value. I've used a bounding box of 3 by 3 pixels to retain the pixels with high surface displacement adjacent to a low surface displacement. A lower median filter can also retain large contrasting values between adjacent pixels to easily identify surface ruptures. A limit on the displacement was also used in this research to limit the range of surface displacement in the final result. This is used to limit extremely large surface displacement that does not have a physical meaning such as decorrelation between the master and slave images (Leprince et al., 2007). The data were further down sampled (lowering sampling rate) with 3 pixels in range and 2 pixels in azimuth. The resolution for the surface displacement of the combined pairs is ~300 m (305.6 m) per pixel from the original 30 m per pixel in the SAR image. The decreased resolution saves processing time and uses lesser computing power. A pre-mainshock sub-pixel offset was performed to determine the surface displacement around the region before the mainshock.

Track	Master (yyyy/mm/dd)	Slave (yyyy/mm/dd)	Days after Mainshock
A9	2018/02/23	2018/03/07	9
A82	2018/02/16	2018/02/28	3
D133	2018/02/19	2018/03/03	6

Table 2: Track A represents ascending track and D represents a descending track (followed by the track number). Also shown are the dates of the SAR images prior (master) and after the earthquake (slave). The duration (days) after the mainshock (25th February) is also listed.

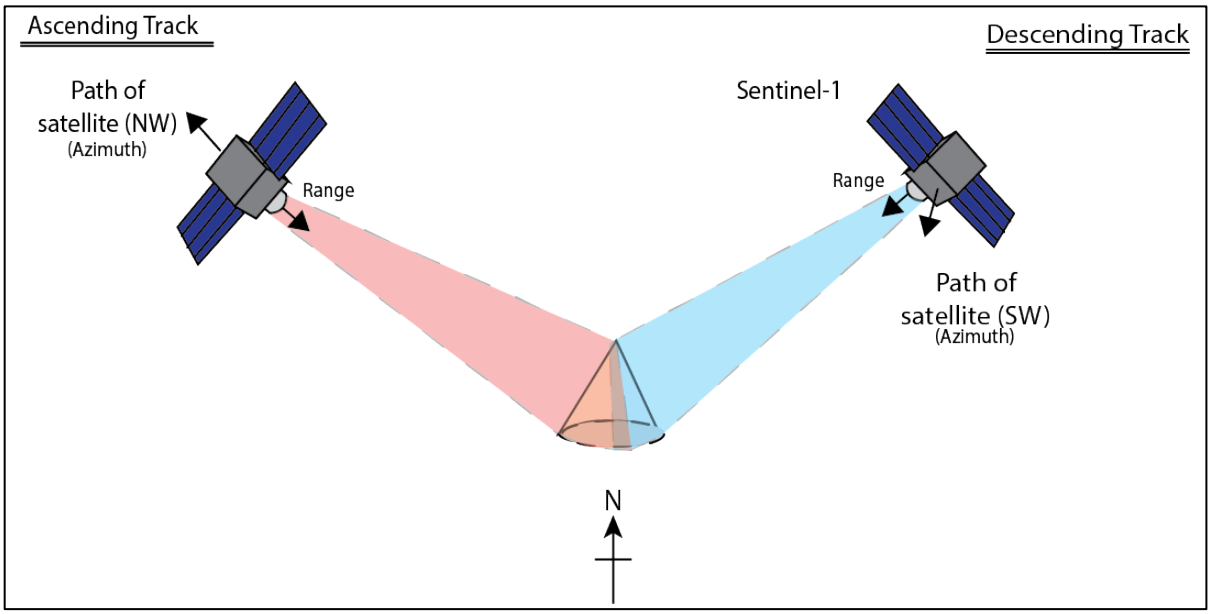

Figure 7: Illustration of an ascending track and descending track with the labeled directions of azimuth (direction of the satellite) and range (line-of-sight). Azimuth and range are perpendicular to each other. The flight path of the satellite is the same direction as the azimuth.

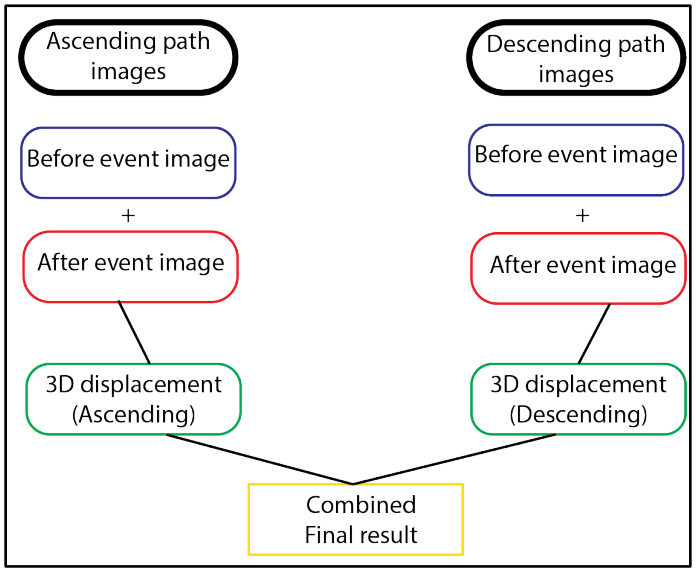

Figure 8: Simplified chart explaining the acquisition of the SAR images and the processes to the final displacement product.

6.2. Fault slip model

A fault slip model is used to characterize the coseismic deformation of the faults involved in the mainshock. The fault slip model provides the amount of slip at each sub-fault and the surface displacement based on a given fault parameter and constrained by a geodetic surface displacement. In this case, the geodetic surface displacement is from the sub-pixel offset determination. To simplify the explanation of producing the fault slip model, I've simplified the explanation into two parts for this process. The first part is to calculate the equation called Green's function that is needed for the inversion of the fault slip model and the second process is the inversion process.

EDGRN/EDCMP was used to compute Green's function (Wang et al., 2003). The Green's function is an equation used to estimate the surface displacement of faults from model slips of faults at depth (Eqn. 1). A layered half-space model with the crustal parameters of a specific region from CRUST 1.0 was used to produce the Green's function (Laske et al., 2013). The layered half-space model crustal parameters used is referenced from the point, 6.5 S, 143.5 E (Table 3). A layered half-space model demonstrates a more realistic approach albeit with a coarser value than the elastic half-space from Okada (Hill et al., 2012).

The Green's function is calculated using the formula:

$$d_{est} = Gm \qquad (1)$$

where G is the Green's function, d_{est} is the estimated surface displacement (m), m is the model of the slip at depth.

For the second part of this inversion process, I've estimated the fault parameters to construct the fault slip model. The parameters include the strike, dip, rake, depth of fault, and size of the fault. The fault parameters were varied to determine suitable parameters. The Green's function was incorporated in the process of inversion. In addition, the coseismic surface displacements from the sub-pixel offset are jointly used to better constrain the fault slip model (Yen et al., 2018). To determine the suitable parameters of the faults that were involved in this mainshock, a minimization between the surface displacement of the sub-pixel offset, d_{obs} and the model, d_{est} was used. The fault parameters that show the smallest difference between the modeled surface and observed displacements from the sub-pixel offset will be selected. The horizontal and vertical displacements were used to compare the surface displacements. The horizontal displacement is the resultant vector of the N-S and E-W displacement. A rectangular slipping dislocation was used to produce the fault slip model. I've also tested the fault parameters of finite-fault solution model from USGS to compare the modeled surface displacement with the surface displacement from the sub-pixel offset. The inversion uses the L2-norm to fit the modeled displacement.

Variance reduction (VR) was also used in this research to prevent overfitting or underfitting of smoothing parameters (Eqn. 2) (Huang et al., 2017).

$$\mathrm{VR} = \left[1 - \frac{\Sigma(d-s)^2}{\Sigma d^2}\right] \times 100 \qquad (2)$$

where d represents the observed data and s the modeled data. The smoothing parameter affects the amount of slip on faults. A lower smoothing parameter will result in coarser amounts of slip along the fault and will lower the VR. The smoothing parameter is chosen if the VR adjacent to the highest

VR does not significantly improve the results. The Mananda Fault was used to test the suitable smoothing parameter for the remaining model fitting. The preferred rake angle for all the fault uses the VR technique too.

The misfit between the modeled and observed displacements were also calculated using a root-mean-square. The misfit is used to determine the suitable parameters that were required for the faults. A lower misfit indicates a better fitting of modeled displacement to the observed displacement.

Layers	Vp (km/s)	Vs (km/s)	Depth (km)	Density (g/cm^3)
Sediments	2.50	1.07	0.29	2.11
Crust 1	5.80	3.40	12.67	2.63
Crust 2	6.30	3.62	23.58	2.74
Crust 3	6.90	3.94	33.81	2.93
Upper Mantle	8.01	4.45	100	4.45

Table 3: Crust 1.0 parameters from the 6.5 S, 143.5 E within the Southern Highlands with a mean surface height of 1.190 km. Upper mantle does not require an absolute depth to compute the Green's function as the upper mantle uses the half-space model from Okada, 1985.

7. Results

7.1. Surface displacement

Preliminary analysis using the Interferometric Synthetic Aperture Radar (InSAR) method did not provide consistent results. This is because the dense vegetation scatters the shorter wavelength microwave (C-band) used by the Sentinel-1A that results in decorrelation (Pepe and Calo, 2017).

Two surface ruptures from two separate faults were identified based on the discontinuity of the vertical displacement. The naming of the faults is given based on the closest known geographical locations in published papers. The fault to the east is the Mubi Fault located within the Imbricate Belt and the Mananda Fault is located at in front of the Mananda anticline in the Strongly Folded Belt (Figure 9). The Mubi Fault has the longer surface rupture with an estimated length of ~35 km and the Mananda Fault has the shorter surface rupture with an estimated length of ~22 km. The peak vertical displacement for the Mubi Fault is ~2.1 meters (Figure 10) and the Mananda Fault is ~1.2 meters of peak uplift. The Mananda Fault also has ~3 meters of southward displacement and the Mubi Fault has ~2 meters peak southward displacement (Figure 11). Both faults produce a peak westward movement of ~2 meters (Figure 12). The Mubi Fault also tends to show an almost linear surface rupture and the Mananda Fault shows a curved rupture that follows the topography. Sub-pixel offset results prior to the mainshock did not show any surface displacement around the Papuan Fold and Thrust Belt. Lake Kutubu does not have a reliable surface displacement measurement as water bodies have irregular water surface that causes decorrelation (Leprince et al., 2007). Blue patches indicating high subsidence (>3 meters) in localized areas were identified as landslides (Figure 9). Further discussion regarding the landslides will be discussed later in the paper.

The displacement trend of both faults is not similar as shown in the cross-section view of the vertical displacement (Figure 10). The uplift across the Mubi Fault (transect a-a') occurs throughout a wider region. Whereas, the peak uplift for the Mananda Fault (transect b-b') is located in between 6 km to 7 km and is followed by subsidence at 11 km to 12 km. Subsequently, an uplift of ~0.5 meters is also visible after the subsidence. Both transects used here have a 5 km width.

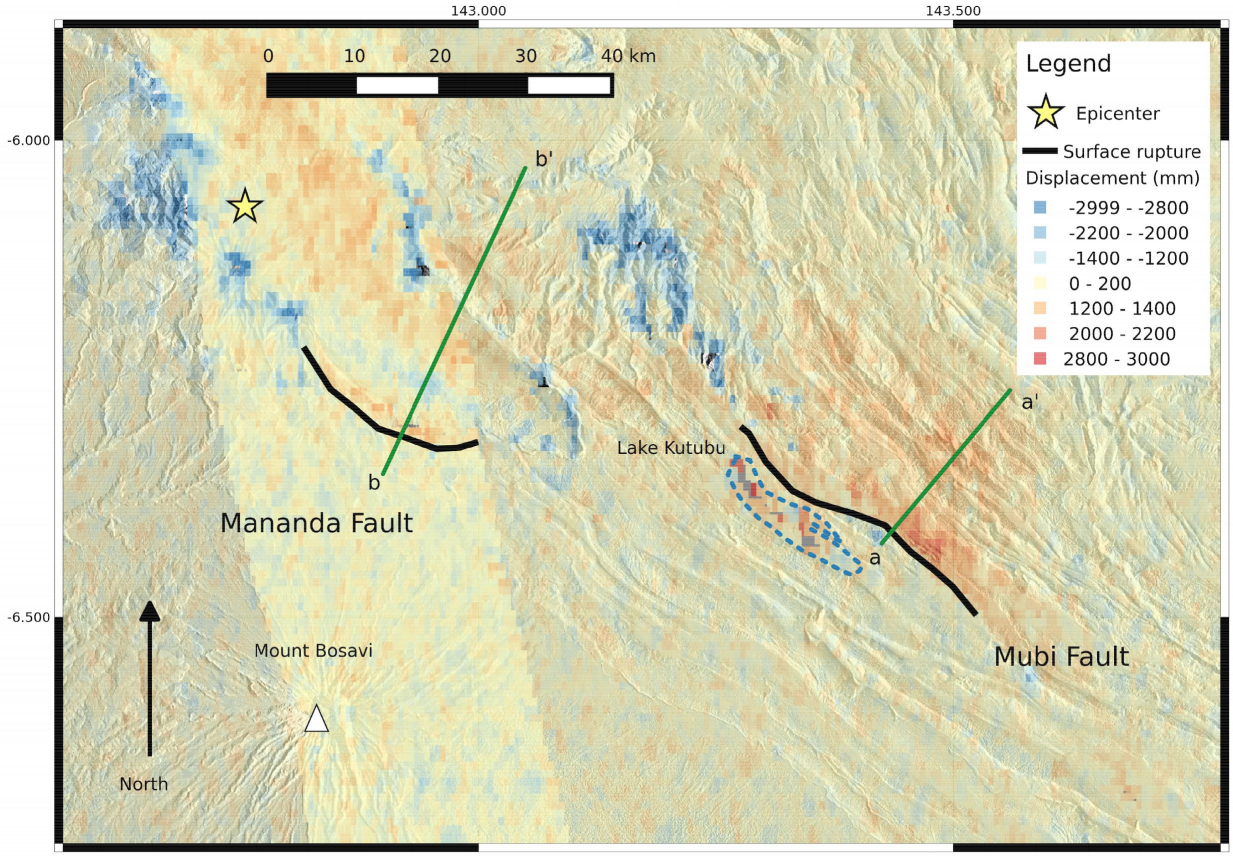

Figure 9: Vertical displacement map of the Southern Highlands. The warm color indicates uplift, cool colors indicate subsidence. The red dot indicates the epicenter of the mainshock. Peak uplift of Mubi Fault is ~2.1 meters and the peak uplift of Mananda Fault is ~1.1 meters.

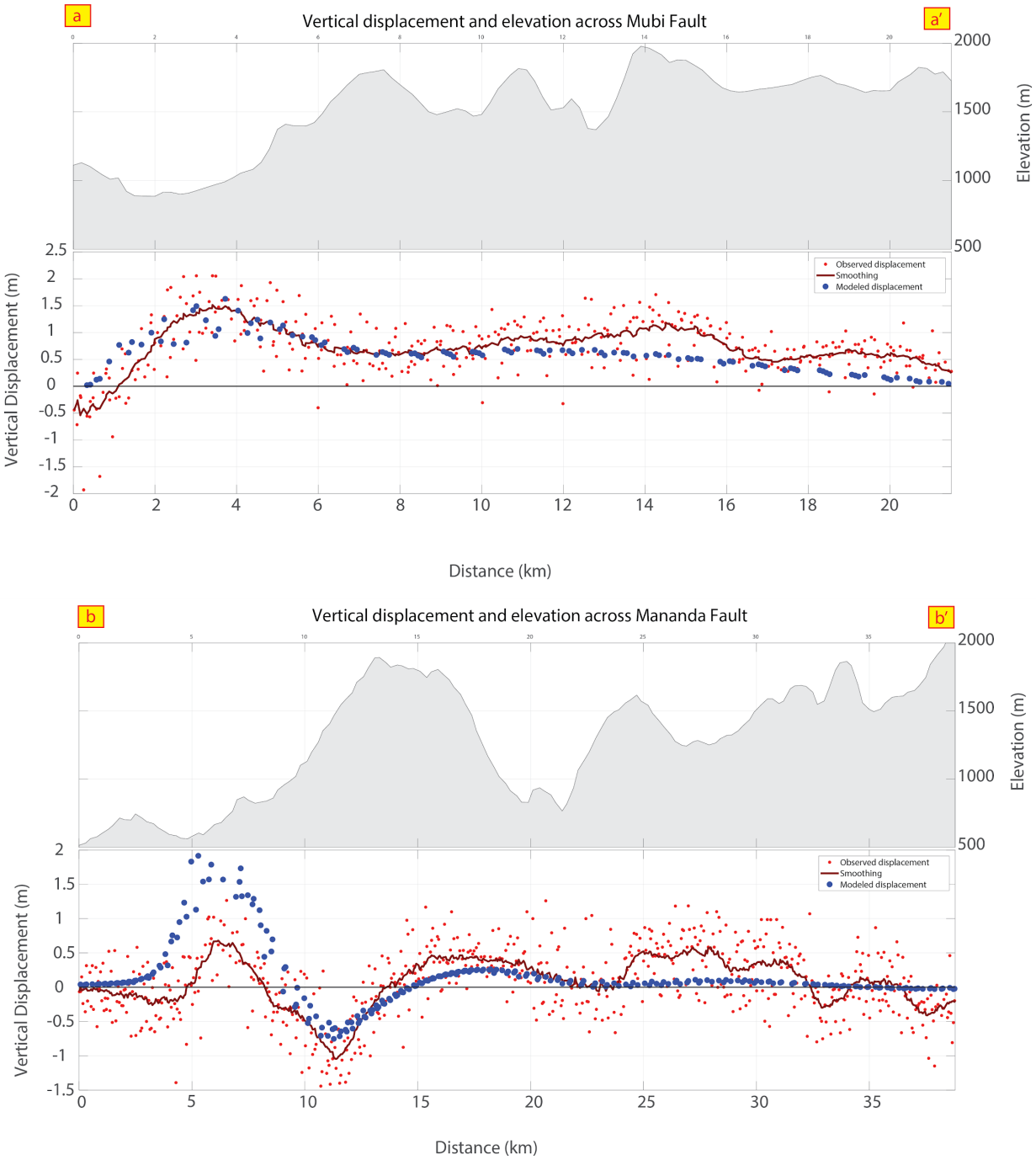

Figure 10: Red dots indicate the displacement values of the observation from the sub-pixel offset method. Blue dots represent the modeled displacement. Red lines are the trend of the observed vertical displacement using a "moving average" at every 15 points. The top figure is the vertical displacement across the transect a to a' (0 km to 24 km). The bottom image is the vertical displacement across the transect b to b' (0 km to 39 km) plotted with their respective elevations obtained from GeoMapApp. Landslides were identified around 21 to 24 km in the cross-section displacement of Mananda Fault.

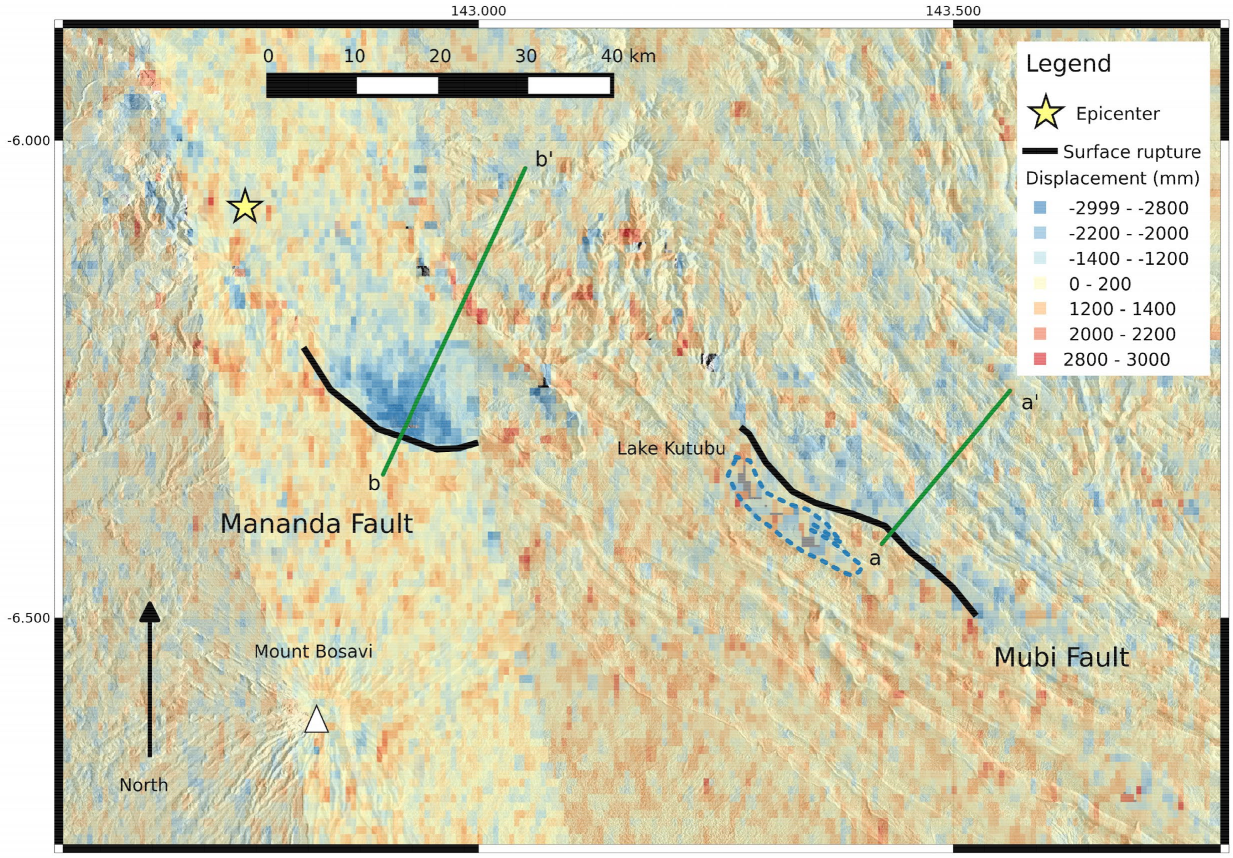

Figure 11: North-south displacement of the Southern Highlands. Warm colors indicate northward movement, cool colors indicate southward movement. Peak southward displacement of the Mananda Fault is ~3 meters and the Mubi Fault is ~2 meters.

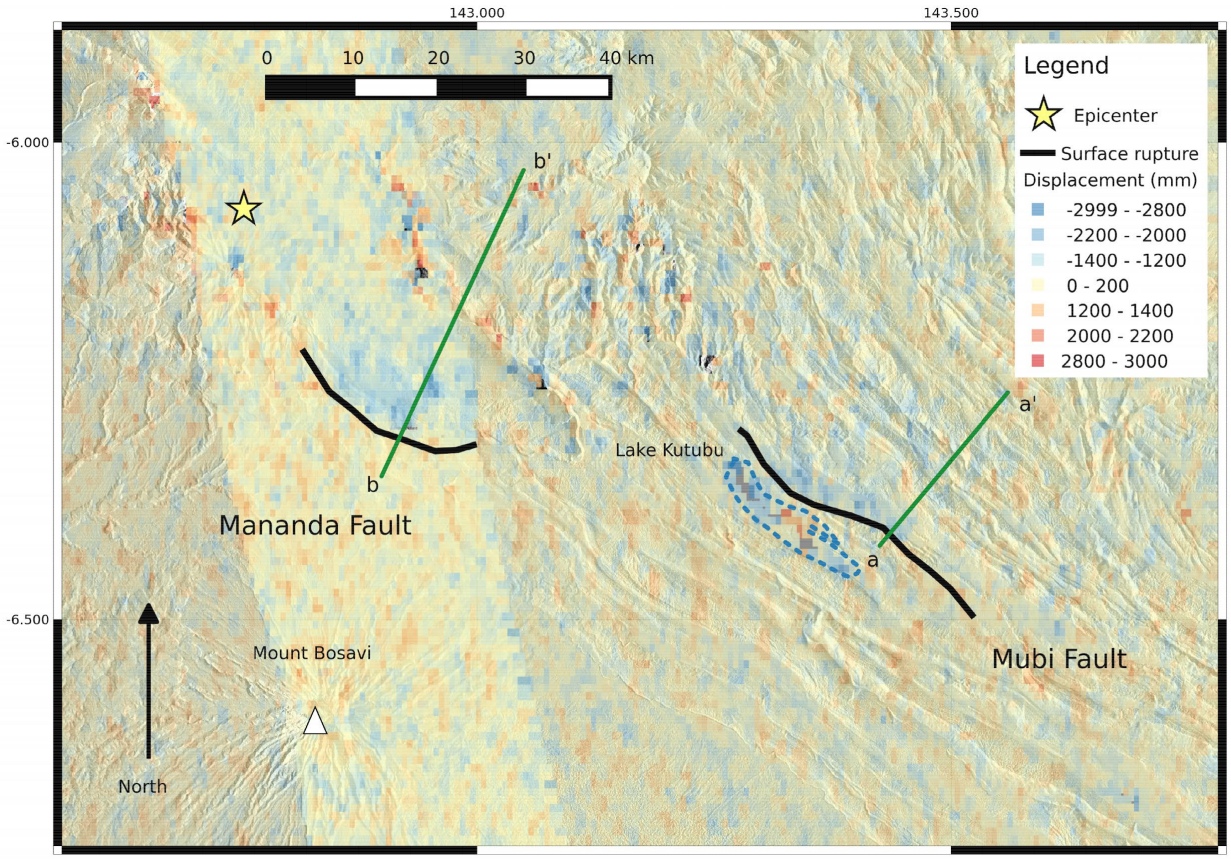

Figure 12: East-west displacement of the Southern Highlands. Warm colors indicate eastward movement, cool colors indicate westward movement. Both ruptures register a peak westward displacement of ~2 meters.

7.2. Identification and removal of landslides

The landslides were first verified using two interchangeable methods. The primary method is to use 1-month mosaic optical imageries from PlanetLab and compare it to the observed vertical displacement results. Landslides can be identified as brown patches (exposed soil) that occurred after the event and landslides are usually visible for months to years. The optical images after the event were between March 2018 to May 2018 and the image before the event prior to March 2018. This method was successfully used to verify that the subsidence at 21 km to 24 km of the cross-section of Mananda Fault was landslides (Figure 13). Also, an ~2 meters of landslide subsidence can be verified at the start of Mubi Fault from 0 km to 2.5 km. The other method would be to use the modeled vertical displacement to distinguish the landslides as the model tends to only produce displacement caused by the faults only. Such as, landslides have high subsidence in the observed displacement but with no subsidence in the model. QGIS was used to remove the landslide displacement, working with a scale of 1:250000. Only landslides with 5 km^2 or larger area with near to the surface ruptures were removed (Figure 13). Displacement along Lake Kutubu was also removed.

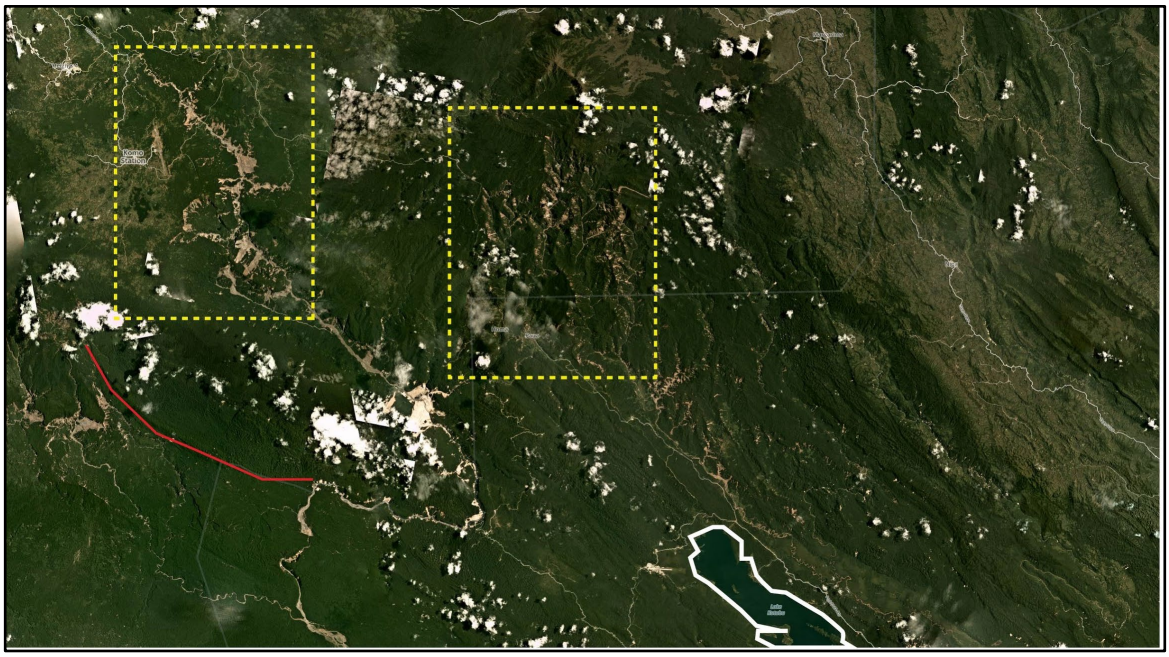

Figure 13: The 1-month mosaic of optical imagery from PlanetLab. The dashed boxes show example areas of landslides that were verified using the optical imagery. Lake Kutubu is highlighted by the white line at the bottom of the image. The Mananda Fault surface rupture is highlighted in red.

7.3. Fault Slip Model

Fault parameters from the USGS finite fault solution did not provide a good fit when compared to the surface displacement of the sub-pixel offset over the region. The peak uplift from the USGS fault parameters exhibited vertical and horizontal displacement values of ~1 meter. Furthermore, the strike of the fault provided by USGS did not line up with the fold-and-thrust belt structure towards the east as it is intended to satisfy the discrepancies of surface displacement from potential faults involved. Thus, two faults with surface rupturing faults were used to explain the surface features observed.

The best-fit dip angle for Mubi Fault was estimated at 35° and Mananda Fault was estimated at 15°. The Mubi Fault has a fault size of 70 km by 18 km, along strike and along dip and Mananda Fault has a fault size of 78 km by 36 km (Table 4). The dimension of subfaults in this research are discretized to 2 km by 2 km. The peak slip of the fault is located along the top 6 km of the Mananda Fault and is ~6.04 meters (Figure 14). The Mananda Fault extends to a depth of ~8.98 km and Mubi Fault extends to a depth of ~9.77 km (Figure 15).

The modeled vertical displacement of the Mubi and Mananda Faults show a similar trend to the observed vertical displacements (Figure 10). The peak uplift of the modeled displacement across the Mubi Fault is ~1.5 meters (2.1 meters in observed) and the Mananda Fault is ~2 meters (1.1 meters in observed). The Mubi Fault has a peak of ~0.5 meters of southward displacement with a peak of ~0.8 westward displacement. The Mananda Fault has a peak of ~1.7 southward displacement and a peak of ~1.5 westward displacement. The model does not estimate the magnitude of the displacement of the landslides as they were triggered by the mainshock. The cross-section plots modeled displacement values within a 3 km width, non-peak displacement values were also plotted on the cross-section that displays the irregular uplift values. The shallower dip angle of the Mananda Fault exhibit subsidence adjacent to the peak uplift in the observed and

modeled displacement. Further investigation using the optical imagery also verified that no landslides were detected within this region.

As there is a lack of published data on the structural geology of the region of interest. The detachment fault was estimated at a length of 130 km and a width of 40 km to connect the two faults (Table 4). The depth of the detachment fault starts at 8.9 km to connect with both faults and extends to 12.8 km. Here, I've used a dip angle of 6° as determined by Hill et al., (2010). The combined faults have an accumulative seismic moment of 9.1311×10^{26} dyne.cm (9.1311×10^{19} Nm) that is equivalent to M_w 7.24. The mean slip of the combined faults is ~72 cm. A smoothing parameter of 8.95×10^{-6} based on fitting of the Mananda Fault. The combined faults have a VR of ~12.8%. For comparison, the VR of sub-pixel offset in this study is lower than another study of the 2010 M_w 7.2 El Mayor-Cucapah earthquake at 51% (Huang et al., 2017).

The vertical displacement has a misfit of 0.35 meters and the resultant horizontal displacement has a misfit of 0.73 meters. The misfit for east-west displacement is 0.49 meters and north-south displacement has 0.67 meters. As for comparison, the surface displacement with the inclusion of landslide displacement has a higher misfit compared to the removed displacements. The vertical misfit was 0.43 meters and horizontal displacement has a misfit of 0.74 meters.

Parameters	Mubi Fault	Mananda Fault	Detachment fault
Strike, Dip, Rake	308, 35, 90	305, 15, 85	307, 6, 90
Size (along strike, dip) in km	70 km, 18 km	86 km, 34 km	130 km, 40 km
Subfaults (strike, dip)	35, 9	43, 17	65, 20
Starting depth	0.8 km	0.7 km	8.9 km

Table 4: Best-fit fault parameters for Mubi Fault, Mananda Fault, and the detachment fault. The subfaults were discretized into 2 km by 2 km.

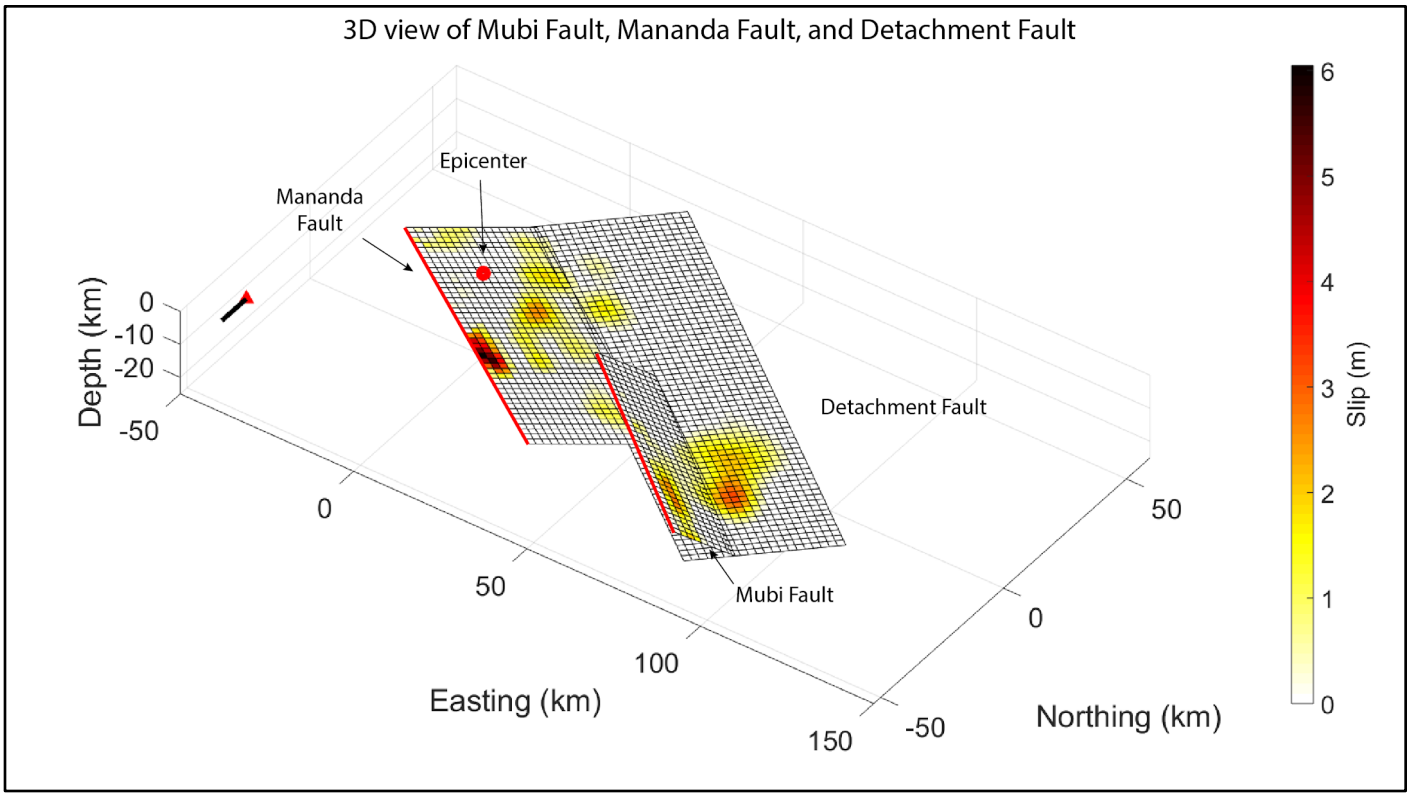

Figure 14: The expected fault slip model of the Mubi Fault, Mananda Fault, and detachment fault. Darker color indicates a higher amount of slip. The epicenter is located at 6.070°S 142.754°E as estimated by USGS and is represented with a red dot located on Mananda Fault. The red line indicates the updip direction of the faults.

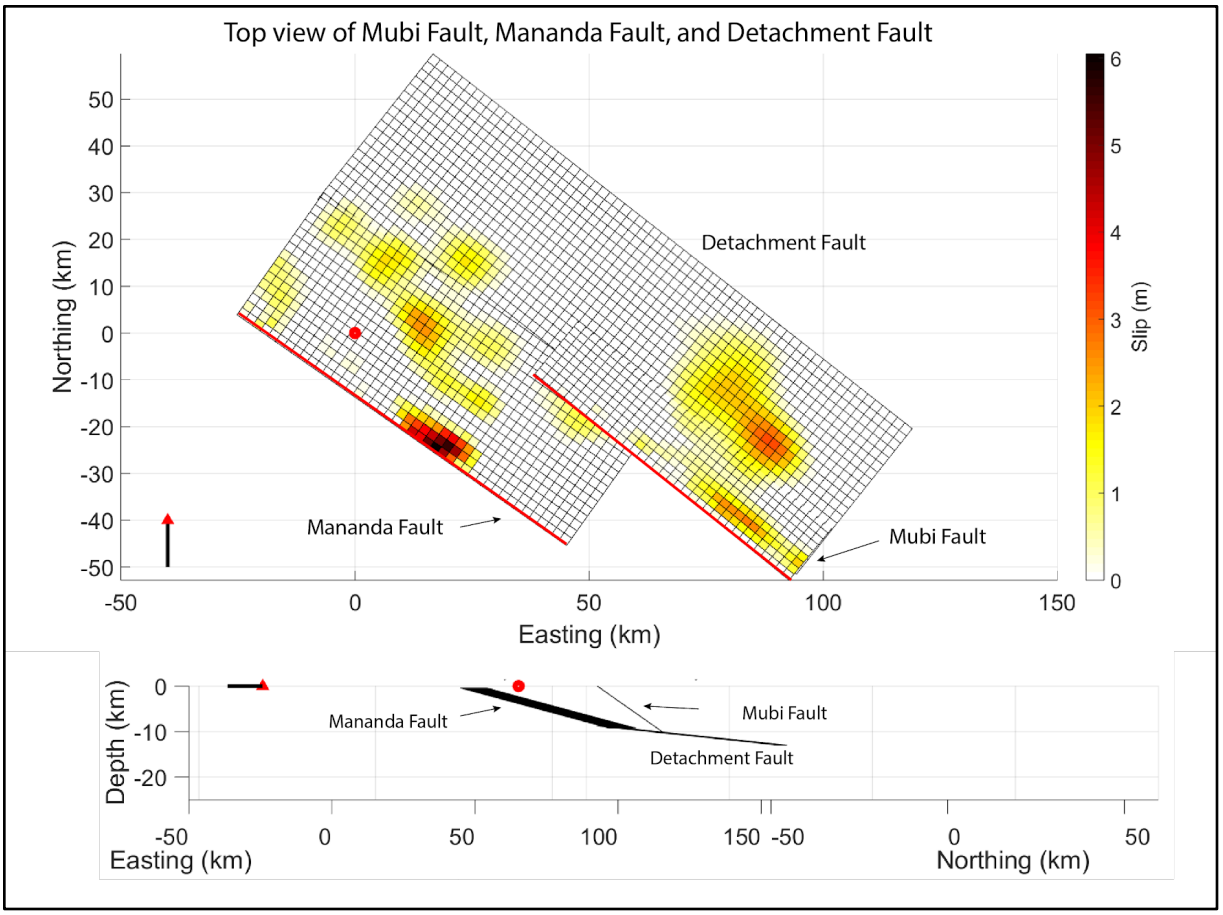

Figure 15: Top view and cross-section view of the faults involved in the mainshock. The red dot indicates the epicenter of the mainshock. The peak slip of ~6.04 meters is located at the top 6 km of the Mananda Fault.

8. Uncertainty

The resolution of SAR images is approximately $\frac{1}{20}$ of pixel size (20 m) or approximately 1 meter (Leprince et al., 2007; Michele et al., 2010; Huang et al., 2017). The measured minimum surface displacement that can be distinguished from the background noise is ~1 meter for this research (Figure A-10). The root mean square (RMS) for the surface displacement is calculated using the root mean square of an area of the background that does not have any surface displacements (Figure A-18). The RMS of the observed vertical displacement is approximately 0.26 meters, the observed east-west displacement is approximately 0.43 meters and the observed north-south displacement is approximately 0.56 meters.

A checkerboard test was used to determine the robustness of the slip on the faults that were resolved at depth (Figure 16). The checkers were set with a grid of 10 km by 10 km. The max slip used for the checkerboard was fixed at either 0 meters or 4.1 meters. The recovery model indicates the degree of recovery from the checkerboard synthetic data. Mananda Fault has a good resolution at shallow to intermediate depth. Whereas, the Mubi Fault has a lower resolution with depth and towards the west. The detachment fault also does not have a well-constrained resolution at depth. The estimated max depth of with a high resolution is ~8 km.

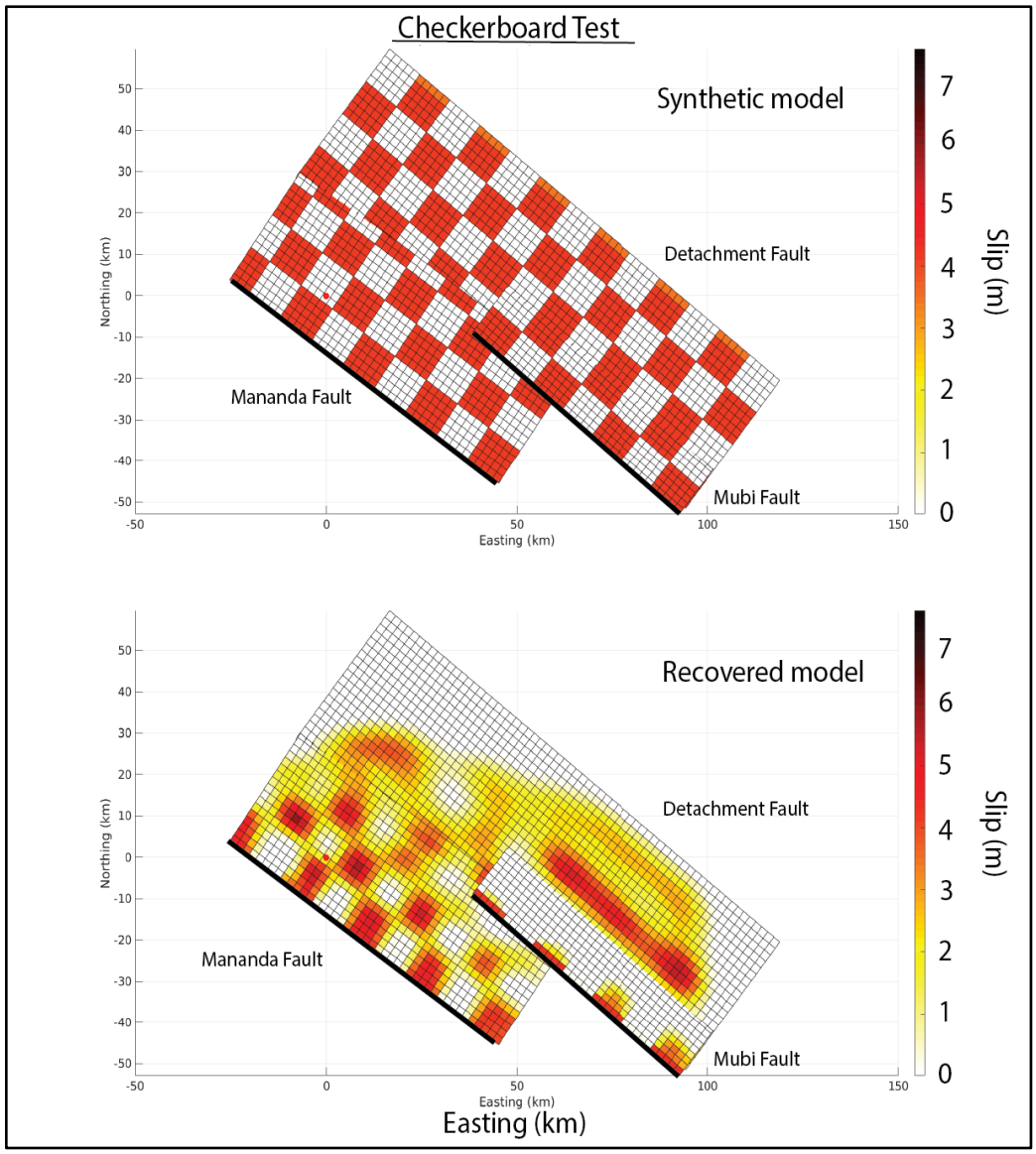

Figure 16: Checkerboard test of the fault models. The checkerboard consists of either 0 (white) or 4.1 (red) meters of slip. The checkerboard test is done with forward predicting surface displacement same as pixel tracking sampling from the synthetic slip distribution. The recovered model is estimated using the synthetic surface displacements. Black lines indicate the updip direction of the faults. The red dot indicates the expected epicenter of the mainshock.

9. Discussion

The two surface rupturing faults (Mubi Fault and Mananda Fault) trend in the NW-SE direction with faults dipping in the NE direction is consistent with the findings of Ripper and McCue (1983). The slight change in the strike direction aligns with the topography. Based on the observed displacement, the surface rupture of the Mubi Fault is located closer to the hinterland and Mananda Fault is located at the frontal part (towards south) of the Strongly Folded Belt. The Mubi Fault is located closer to the hinterland, within the Imbricate Belt. Faults closer to the hinterland tend to have steeper dip angles compared to the faults in the frontal part of the deformation. This also

explains the differences in surface displacement between the two rupturing faults. The steeper fault will have a higher vertical displacement than horizontal displacement and a gentle fault will produce a more significant horizontal displacement than vertical displacement. None of the faults exhibit characteristics of a backthrust fault. Both faults also exhibited a southwest thrusting fault that agrees with the proposed idea of Davies (1979).

The slip is expected to propagate along the detachment fault from the west to the east given that the epicenter is located at the west and the surface ruptures were located at the east. Furthermore, the surface rupture of the Mananda Fault and Mubi Fault tends to trend with the topography. This indicates a tendency of future rupture along the same fault or adjacent (Figure 18). However, further studies are required to better understand the structural geology and potential seismic hazards in the Papuan Fold and Thrust Belt.

As the Mananda Fault and Mubi fault are not in contact with each other. A detachment fault was included in this study to evaluate the idea of slip transfer across two distinctly different fault structures. The detachment fault did not have a strong influence on surface displacement as compared to the Mubi and Mananda Faults (~3 meters of slip on the detachment fault). This is due to the detachment fault is being located deeper below the surface compared to the surface rupturing faults.

Furthermore, the max depth of a good recovery is ~8 km below the surface based on the checkerboard test. The lack of recovery at greater depths and the lack of studies on the structural geology between Mubi and Mananda made constraining the detachment fault structure difficult. Besides that, the hypocenter of the mainshock is not well constrained with different agencies providing different hypocenters with a separation from ~4 km to ~35 km apart and the depth of the hypocenters was also not well-constrained.

The residual vertical displacement indicates there are still uplift behind the Mananda Fault (Figure 17). Furthermore, the magnitude of the mainshock is smaller compared to seismic data interpretation from multiple agencies. This suggests that there could be a missing fault that did not produce a surface rupture in this model. One possibility of the location is that behind the Mananda Fault with a steeper dip angle compared to Mananda Fault. This proposed fault is expected to produce more significant uplift.

Moreover, the rake of the faults was determined using the VR as the changes of surface displacement and is too small to be observed. The preferred dip angle of the faults was not based on the VR as it shows that smaller the dip angle will result in a higher the VR. This includes dip angles of the faults that involved a higher misfit of surface displacement between the modeled and observed results. The best-fit fault parameters also have a lower residual displacement. This is more evident with the horizontal displacement, a resultant of east-west and north-south displacement.

Different geographical location can yield different VR values. The lower VR values are likely to be influenced by the environment. A study of the 2010 El Mayor-Cucapah that was located in Baja, California by Huang et al., (2017) was a desert with less vegetation. An area with less vegetation will have a higher correlation value compared to a forested region as the microwaves were scattered arbitrarily by vegetation. This suggests that the sub-pixel offset method has a lower VR value than InSAR due to a lower resolution of image acquisition. The correlation between the elevation profile and the surface displacement indicate that in certain areas across the transects, the elevation and displacement are correlated. This means that these areas of displacements were

not entirely real surface displacement caused by the earthquake but by the topography (Figure 19). Although there were aftershocks of M_w 6 to M_w 6.7 included in the region. The energy of the M_w 6.7 aftershock is still lower than the mainshock (<16%).

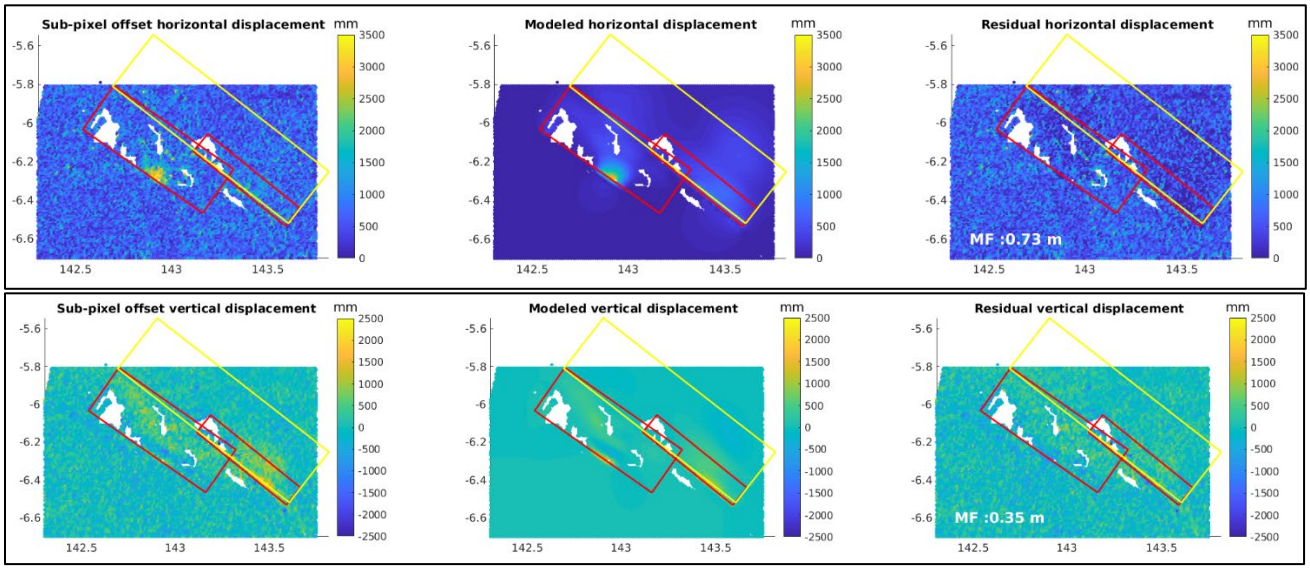

Figure 17: Comparison of observed and modeled surface displacement. The residual is the difference between the observed and modeled displacement. The top row is horizontal displacement which includes North-South and East-West components. The red box outlines the Mubi Fault and Mananda Fault. The yellow box outlines the detachment fault. Misfit (MF) of the residual horizontal and vertical displacement is shown here.

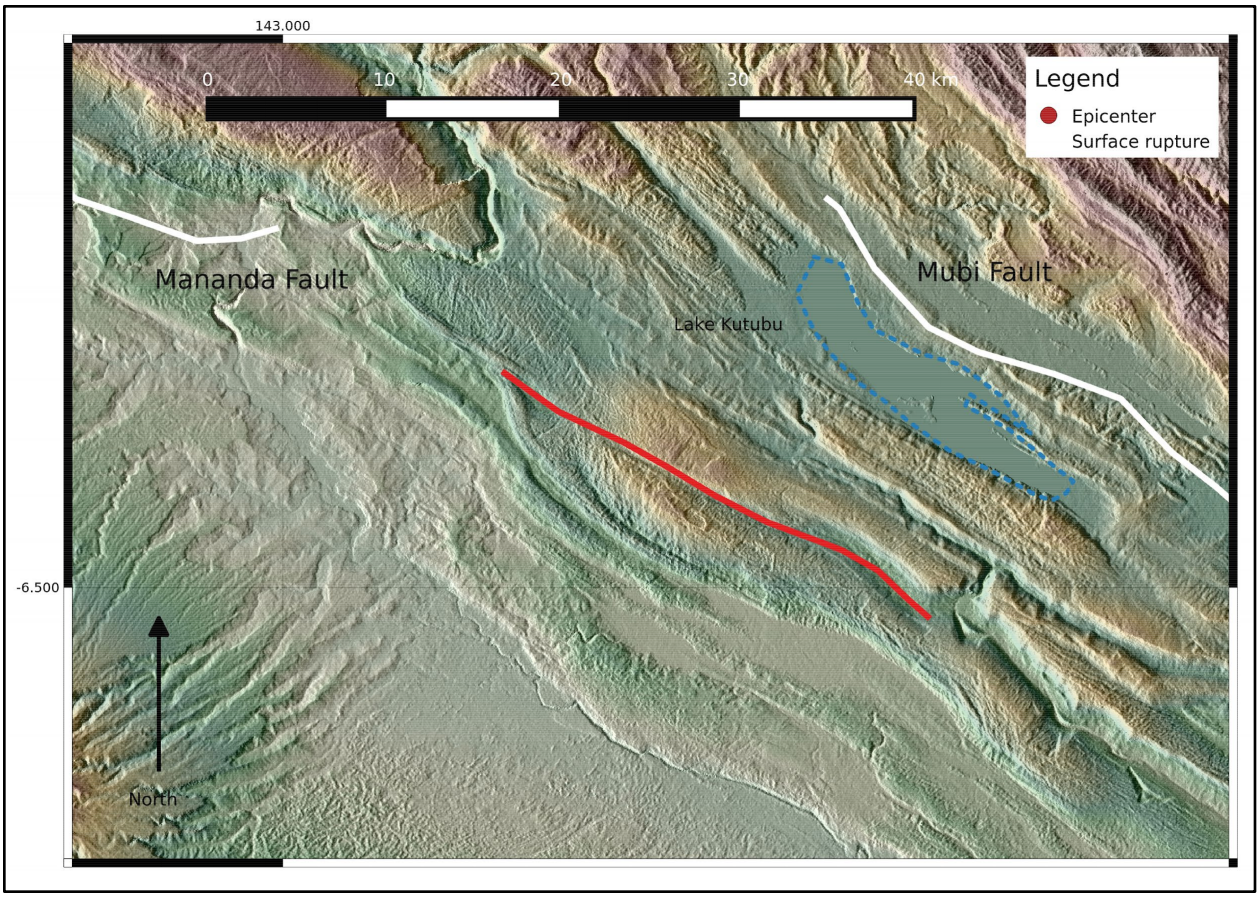

Figure 18: Close up view of the frontal structure in the Southern Highlands. The red trace is the possible surface rupture trace along the topography for future events. White trace is the surface rupture that was identified using the sub-pixel offset method. The topography is from the NASA Shuttle Radar Topography Mission (SRTM) of 1 arc second.

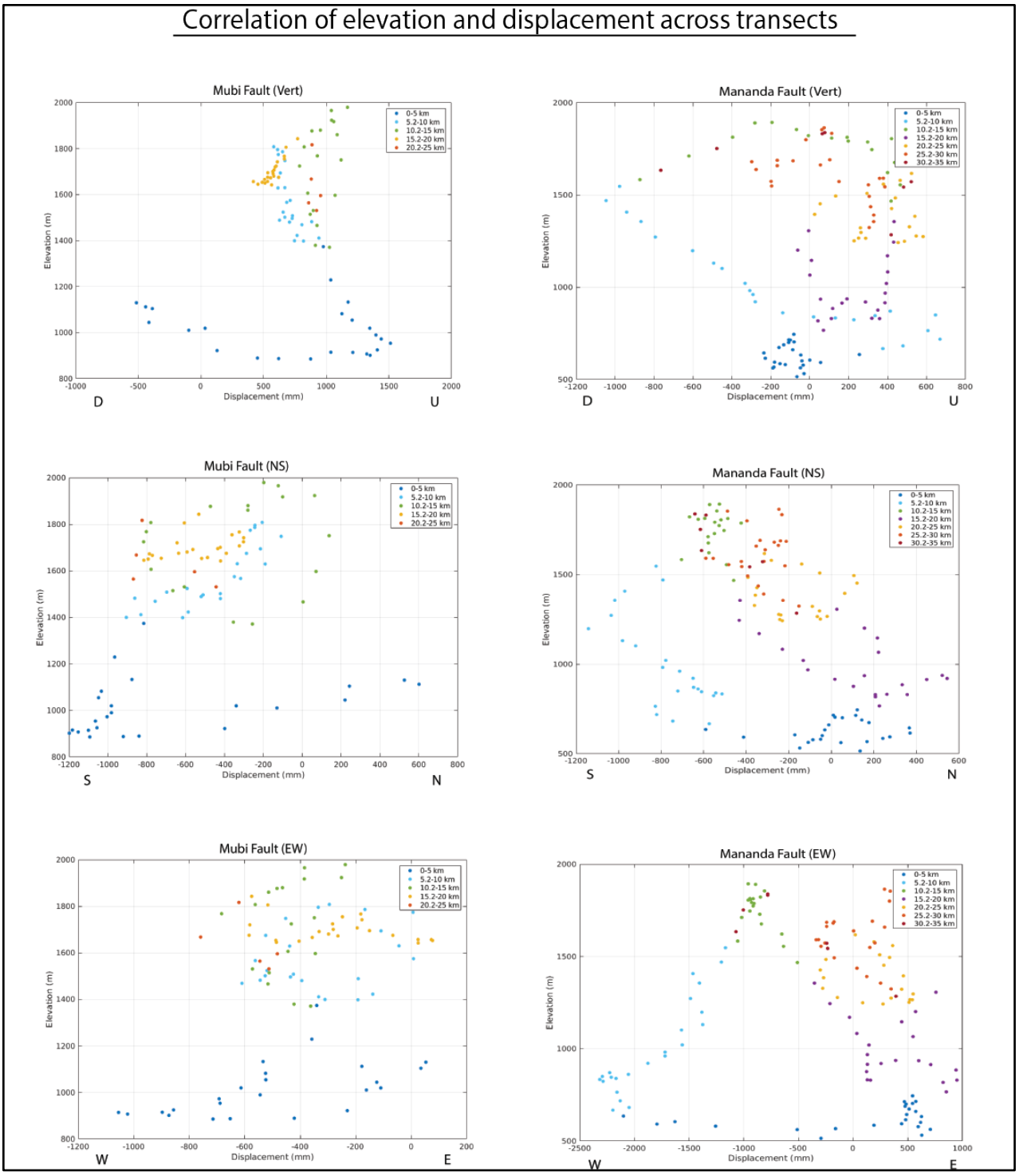

Figure 19: Correlation plot between elevation and displacement across transects. The points of the transects are color-coded according to the distance. The x-axis represents the displacement (mm) and Y-axis represents the elevation (meters) along the transect of the Mubi and Mananda Fault.

10. Broader Impact

The sub-pixel offset successfully detected landslides on top of the surface ruptures of the faults. The landslides were identified using a comparison between optical images from Planet Labs. Landslides also tend to have high subsidence in smaller, localized area. Most of the estimated subsidence of landslides is ~4 meters with the highest subsidence of ~5.9 meters (Figure 20). Several landslides identified here showed evidence of past landslide activity or are in areas of high slopes.

The ability to identify landslides and surface ruptures showed that the sub-pixel offset method can be highly valuable for search and rescue operations. Rescue operations in densely vegetated regions can utilize this method to determine accessibility or assess damages over a large region in a cost-effective way. This method can be used to strategize rescue efforts to provide aid because many of the towns and villages are sparsely located within the forest and it will require a tremendous amount of time and effort to attend every one of them. Furthermore, aerial mapping from Unmanned Aerial Vehicle (UAV) can then be deployed to analyze a specific area based on the analysis from the sub-pixel offset. Airborne and terrestrial Light Detection and Ranging (LiDAR) can also be deployed in the future to complement the results from the sub-pixel offset (Nissen et al., 2014). LiDAR has a higher precision that is useful to analyze morphological features from landslides and surface scarps (Jaboyedoff et al., 2012).

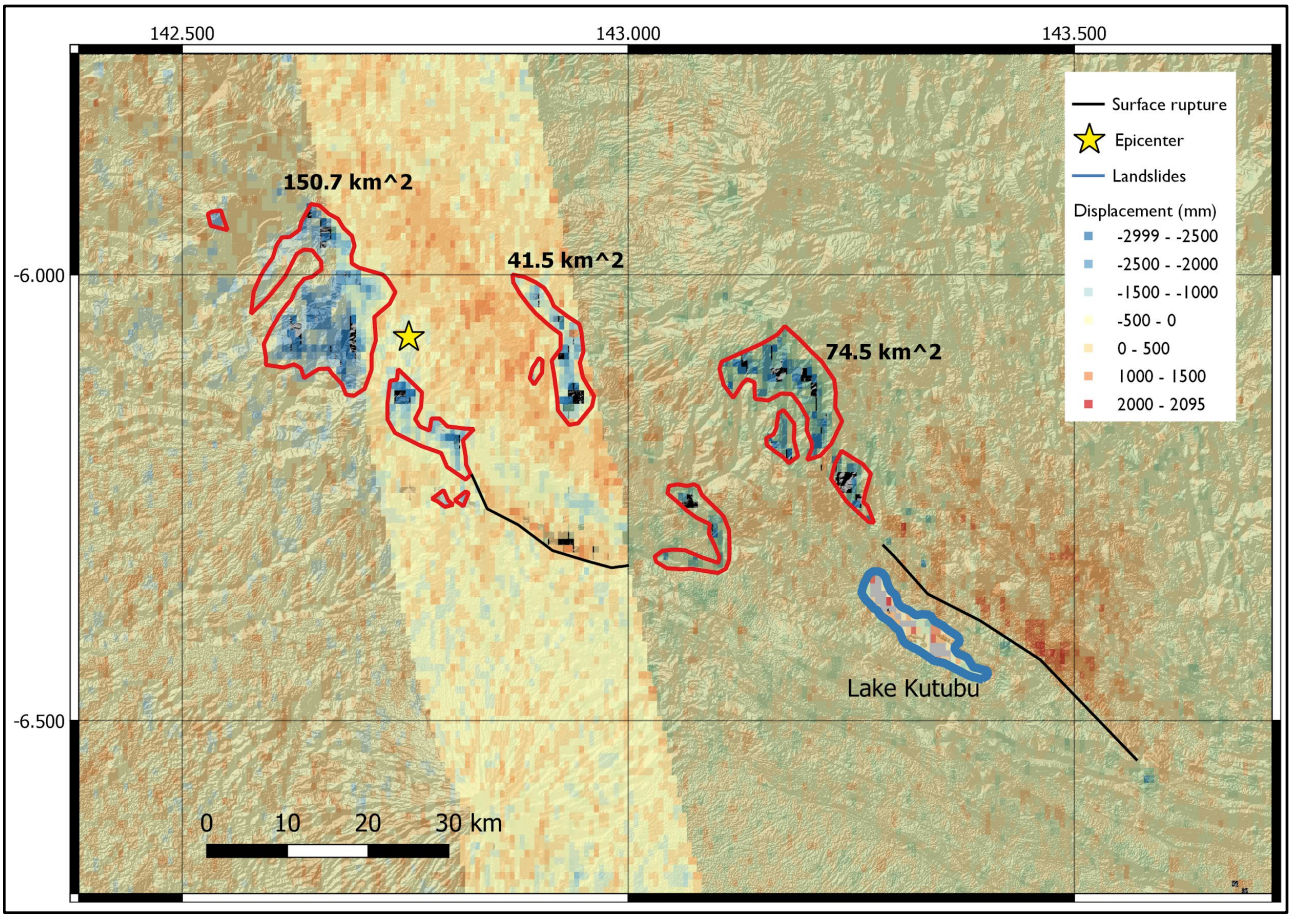

Figure 20: Vertical displacement of landslides layered over topography. Estimated areas of large landslides (highlighted in red) are indicated with the dimensions in km^2. Lake Kutubu is also removed and highlighted in blue. For comparison, Washington DC has a total area of 177 km^2. SNR was not used here to produce the actual displacement of the landslides.

11. Summary

Overall, the results from the fault model agree with the proposed hypothesis. Large magnitude earthquakes are common in the northern region of Papua New Guinea due to the high rate convergence rate between Pacific and Australian Plates. On the 25th of February, an M_w 7.5 earthquake struck the Papuan Fold and Thrust Belt in central Papua New Guinea. This was the largest magnitude earthquake that has been recorded in the region. The fault structure was not constrained precisely due to the lack of a dense network of seismic stations and the absence of active GPS stations. A satellite geodetic method known as the sub-pixel offset method was used to constrain the fault structure within the Southern Highlands of the Papuan Fold and Thrust Belt. The fault slip model constrained by the sub-pixel offset displacements showed that two faults were required to fit the surface ruptures. The peak vertical displacement for Mubi Fault (eastern rupture) is ~2.1 meters and ~1.1 meters for Mananda Fault (western rupture). Whereas the horizontal displacement for Mubi Fault is ~2 meter and ~3 meters for Mananda Fault. The Mubi Fault is expected to be 70 km by 18 km fault striking at 309°, dipping at 35°. The Mananda Fault is expected to have a fault size of 86 km by 36 km striking at 305°, dipping at 15°. The faults in the Papuan Fold and Thrust Belt are southward thrusting faults with a geometry of NW-SE consistent with the suggestion by Ripper and McCue (1983). A detachment fault was also expected with a fault size of 130 km by 40 km. The detachment fault was used to explain the transfer of slip from the Mananda Fault to the Mubi Fault. The peak slip is ~6 meters located in the top 6 km of the Mananda Fault, 0.7 km below the surface. It is also acknowledged that the detachment fault might play a significant role in this earthquake. However, without seismic data closer to the source, it would be difficult to constrain the earthquake. Conclusively, the sub-pixel offset is an effective method to provide a 3D surface displacement to understand the fault structures involved in an earthquake. This method can also be used in densely vegetated regions by first responders to obtain a quick damage assessment map and effectively prioritize their rescue efforts in vast regions.

Bibliography

Abers, G., and McCaffrey, R., (1988), Active deformation in the New Guinea fold-and-thrust belt: Seismological evidence for strike-slip faulting and basement-involved thrusting, *Journal of Geophysical Research,* v. 93, 12,332-13354, doi:0148-0227/88/007B-5097

Anton, L., and Gibson, G., (2015), Earthquake hazard in Papua New Guinea: problems and the way forward, *Proceedings of Australian Earthquake Engineering Society*.

Baldwin, S. L., Fitzgerald, P.G., and Webb, L.E., (2012), Tectonics of the New Guinea Region, *Annual Review Earth Planet Science*, v. 40, 495-520, doi: 10.1146/annurev-earth-040809-152540

Bürgmann, R., (2018), The geophysics, geology and mechanics of slow fault slip, *Earth and Planetary Science Letter,* v. 495, 112-134, doi:10.1016/j.epsl.2018.04.062

Bürgmann, R., Rosen, P, A., and Fielding, E. J., (2000), Synthetic Aperture Radar Interferometry To Measure Earth's Surface Topography And Its Deformation, *Annual Review Earth Planet Science,* v. 28, p 169-209, doi:0084–6597/00/0515–0169

Cai, J., Wang, C., Mao, X., and Wang, Q., (2017), An adaptive offset tracking method with SAR images for landslide displacement monitoring, *Remote Sensing,* v.9, 830, doi:10.3390/rs9080830

Davies, H. L., (1979), Explanatory notes to accompany to Mianmin 1:250 000 Geological Map. *Geological Survey of Papua New Guinea*, v. 79, 27. doi.

Davies, H. L., (2012), The geology of New Guinea - the Cordilleran margin of the Australian continent, *Episodes,* 35(1), 87-102. doi.

Dominguez, S., Avouac, J-P., and Michel, R., (2003), Horizontal coseismic deformation of the 1999 Chi-Chi earthquake measured from SPOT satellite images: Implications for the seismic cycle along the western foothills of central Taiwan, *Journal of Geophysical Research,* v. 108 (B2), 2083, doi:10.1029/2001JB000951

Ghasemi, H., McKee, C., Leonard, M., Cummins, P., Moihoi, M., Spiro, S., Taranu, F., and Buri, E., (2016), Probabilistic seismic hazard map of Papua New Guinea, *Natural Hazards*, v. 81, 1003-1025, doi:10.1007/s11069-015-2117-8

Haghighi, M. H., and Motagh, M., (2017), Sentinel-1 InSAR over Germany: Large-scale interferometry, atmospheric effects and ground deformation mapping, *Zeitschrift fur Geodasie, Geoinformation und Land management,* v. 142(4), 245-256, doi:10.12902/zfv-0174-2017

Heidarzadeh, M., Gusman, A. R., Harada, T., and Satake, K., (2015), Tsunamis from the 29 March and 5 May 2015 Papua New Guinea earthquake doublet (M_w 7.5) and tsunamigenic potential of the New Britain Trench, *Geophysical Research Letters*, v. 42, 5958-5965, doi:10.1002/2015GL064770

Hill, E. M., Borrero, J. C., Huang Z., Qiu, Q., Banerjee, P., Natawidjaja D. H., Elosegui, P., Fritz, H. M., Suwargadi, B. W., Pranantyo, I.R., Li, L., Macpherson, K. A., Skanavis, V., Synolakis, C.E., and Sieh, K., (2012), The 2010 M_w 7.8 Mentawai earthquake: very shallow source of a rare tsunami earthquake determined from tsunami field survey and near-field GPS data, *Journal of Geophysical Research,* v. 117, B06402, doi:10.1029/2012JB009159

Hill, K. C., and Hall. R., (2003), Mesozoic-Cenozoic evolution of Australia's New Guinea margin in a west Pacific context, *Geol. Soc. Australia Spec. Publ.*, 22, doi: 10.1130/0-8137-2372-8.265

Hill, K. C., Lucas, K., and Bradey, K., (2010), Structural styles in the fold-and-thrust belt, Papua New Guinea: constraints from analogue modelling, *Geological Society of London,* 348, 35-56, doi: 10.1144/SP348.3

Huang, M. H., Fielding, E.J., Liang, C., Milillo, P., Bekaert, D., Dreger, D., and Salzer, J., (2017), Coseismic deformation and triggered landslides of the 2016 Mw 6.2 Amatrice earthquake in Italy, *Geophysical Research Letters,* 122, 607-621, doi:10.1002/2016GL071687

Jaboyedoff, M., Oppikofer, T., Abellan, A., Derron, M-H., Loye, A., Metzger, R., and Pedrazzini, A., (2012), Use of LiDAR in landslide investigation: a review, *Natural Hazards*, v. 61, 5-28, doi:10.1007/s11069-010-9634-2

Koulali, A., Tregoning, P., McClusky, S., Stanaway, R., Wallace, L., and Lister, G., (2015), New Insights into the present-day kinematics of the central and western Papua New Guinea from GPS, *Geophysical Journal International*, 202, 993-1004, doi:10.1093/gji/ggv200

Laske, G., Masters, G., Ma, Z., and Pasyanos, M., (2013), Update on CRUST1.0 - a 1-degree global model of Earth's crust, Geophysical Research Abstract, 15, 2658.

Leprince, S., Barbot, S., Ayoub, F., Avouvac, J-P., (2007), Automatic and precise orthorectification, coregistration, and subpixel correlation of satellite images, application to ground deformation measurements, *IEEE Transactions on Geoscience and Remote Sensing,* v. 45(6), doi:0196-2892

Michele. d. M., Raucoules. D., Sigoyer. d. J., Pubellier, M., and Chamot-Tooke, N., (2010), Three-dimensional surface displacement of the 2008 May 12 Sichuan earthquake (China) derived from Synthetic Aperture Radar: evidence for rupture on a blind thrust, *Geophysical Journal International*, v. 183 (3), 1097-1103, doi: 10.1111/j.1365-246X.2010.04807.x

Nissen, E., Maruyama T., Arrowsmith, J. R., Elliot, J. R., Krishnan, A. K., Oskin, M. E., and Saripalli, S., (2014), Coseismic fault zone deformation revealed with differential lidar: examples from Japanese Mw ~7 intraplate earthquakes, *Earth and Planetary Science Letters*, v. 405, 244-256, doi:10.1016j.epsl.2014.08.031

Okada, Y., (1985), Surface deformation due to shear and tensile faults in a half-space, *Bulletin of the Seismological Society of America,* v. 75(4), 1135-1154, doi.

Pepe, A., and Calo, D., (2017), A review of interferometric synthetic aperture radar (InSAR) multi-track approaches for the retrieval of Earth's surface displacement, *Applied Science,* v. 7, 1264, doi:10.3390/app7121264

Ripper, I. D., and McCue, K, F., (1983), The seismic zone of the Papuan Fold Belt, *Journal of Australian Geology & Geophysics*, v. 8, 147-156.

Rosen, P., Gurrola, E., Sacco, G. F., Zebker, H., (2012), The InSAR scientific computing environment, Proc, EUSAR, Nuremberg, Germany, 720 -733

Satake, K., and Tanioka, Y., (2003), The July 1998 Papua New Guinea earthquake: Mechanism and Quantification of unusual tsunami generation, *Pure and Applied Geophysics*, v. 160, 2087-2118, doi:10.1007/s00024-003-2421-1

Tregoning, P., McQueen, H., Little, R., and Rosa, R., (2000), Present-day crustal motion in Papua New Guinea, *Earth Planets Space,* v. 52, 727-730, doi:10.1186/BF03352272

Tregoning, P., and Gorbatov, A., (2004), Evidence for active subduction at the New Guinea Trench, *Geophysical Research Letters,* v. 31, doi:10.1029/2004GL020190

United States Geological Survey, (2018), M 7.5 - 83 km SW of Porgera, Papua New Guinea, https://earthquake.usgs.gov/earthquakes/eventpage/us2000d7q6/executive, Accessed 20th August 2018.

United States Geological Survey, (2018), USGS earthquake catalog, https://earthquake.usgs.gov/earthquakes/search/, Accessed 20th September 2018.

Wallace, L. M., Stevens, C., Silver, E., McCaffrey, R., Loratung, W., Hasiata, S., Stanaway, R., Curley, R., Rosa, R., and Taugaloidi, J., (2004), GPS and seismological constraints on active tectonics and arc-continent collision in Papua New Guinea: Implications for mechanic of microplate rotations in a plate boundary zone, *Journal of Geophysical Research*, v. 109, doi:10.1029/2003JB002481

Wang, R., Martin, F. L., and Roth, F., (2003), Computation of deformation induced by earthquakes in a multi-layered elastic crust - FORTRAN programs EDGRN/EDCMP, *Computers & Geosciences,* v. 29, 195-207, doi:0098-3004/02

Yen, J-Y., Lu, C-H., Dorsey, R. J., Kuo-Chen, H., Chang, C-P., Wang, C-C., Chuang, R.Y., Kuo, Y-T., Chiu, C-Y., Chang, Y-H., Bovenga, F., and Chang, W-Y., (2018), Insights into Seismogenic Deformation during the 2018 Hualien, Taiwan, Earthquake Sequence from InSAR, GPS, and Modeling, *Seismological Research Letters,* doi:10.1785/0220180228

Zhou, X., Chang, E-B., and Li, S., (2009), Applications of SAR Interferometry in Earth and Environmental Science Research, *Sensor*, v. 9, 1876-1912, doi:10.3390/s90301876

Appendix

"I pledge on my honor that I have not given or received any unauthorized assistance or plagiarized on this assignment."

Jeng Hann, Chong

Formula

Mean was calculated using, md = (Σd)/N

The formula used for calculating standard deviation, SD = sqrt ([Σ (d-md)^2] / N)
Where *d* is the data, *md* is the mean of the data, and *N* is the total count of data.

Figures

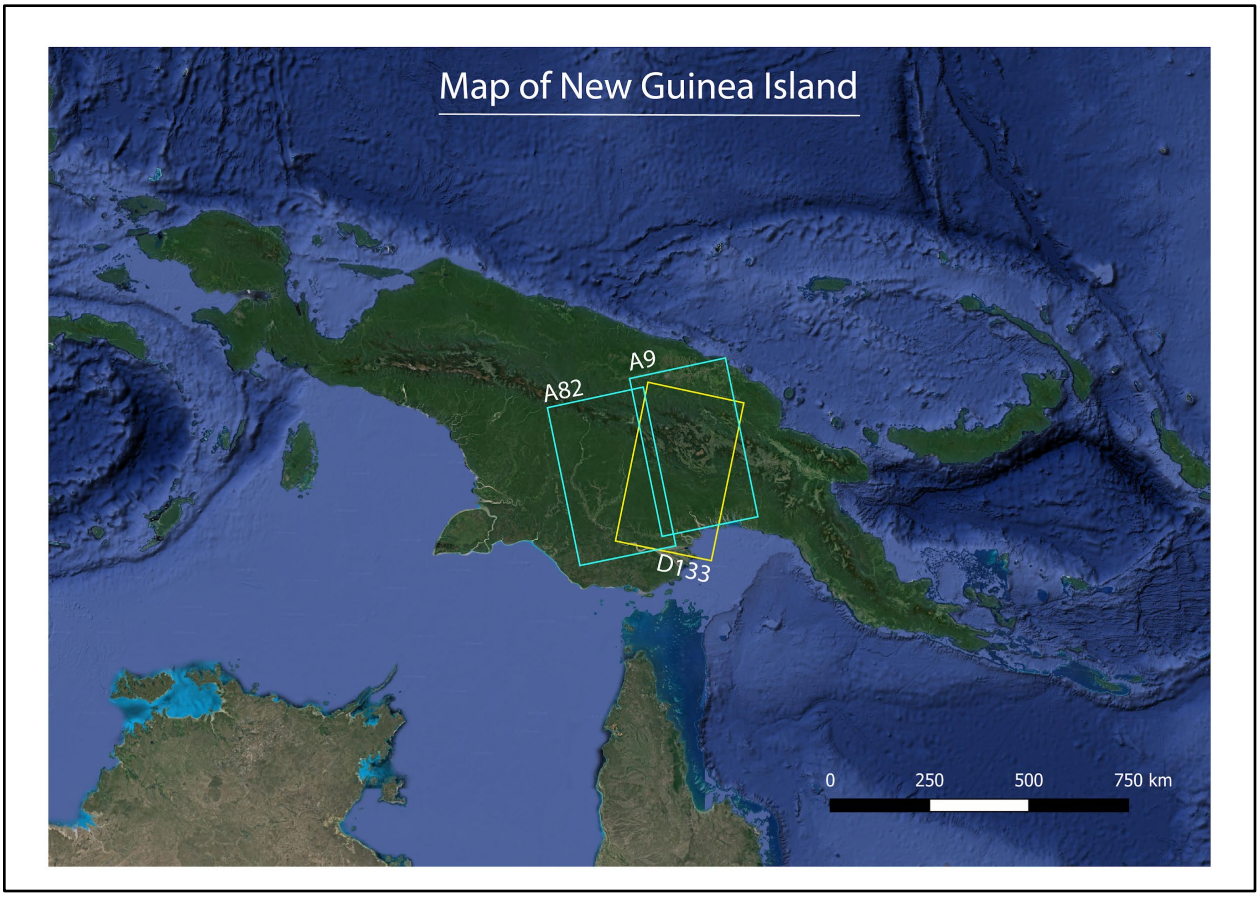

Figure A-1: Map of New Guinea Island with the tracks labeled accordingly. The coverage of the SAR images of descending track (D133) is colored with yellow and ascending tracks (A9 and A82) is colored with blue. A bounding box was used within the outlines for this research.

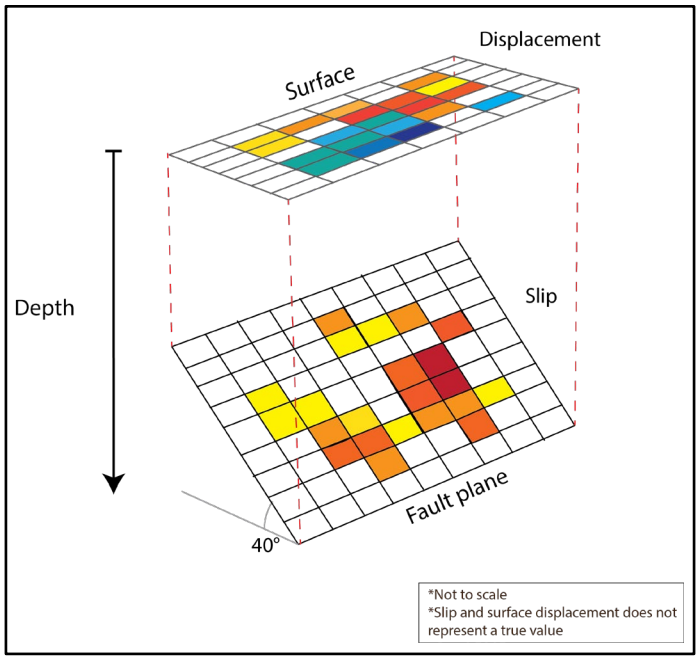

Figure A-2: Illustration of an example of slip on the fault and surface displacement. The fault plane is located below the surface and the sub-faults are indicated with the grid on the fault plane. The surface displacement is located above on the surface with grids indicating areas with a certain amount of surface displacement.

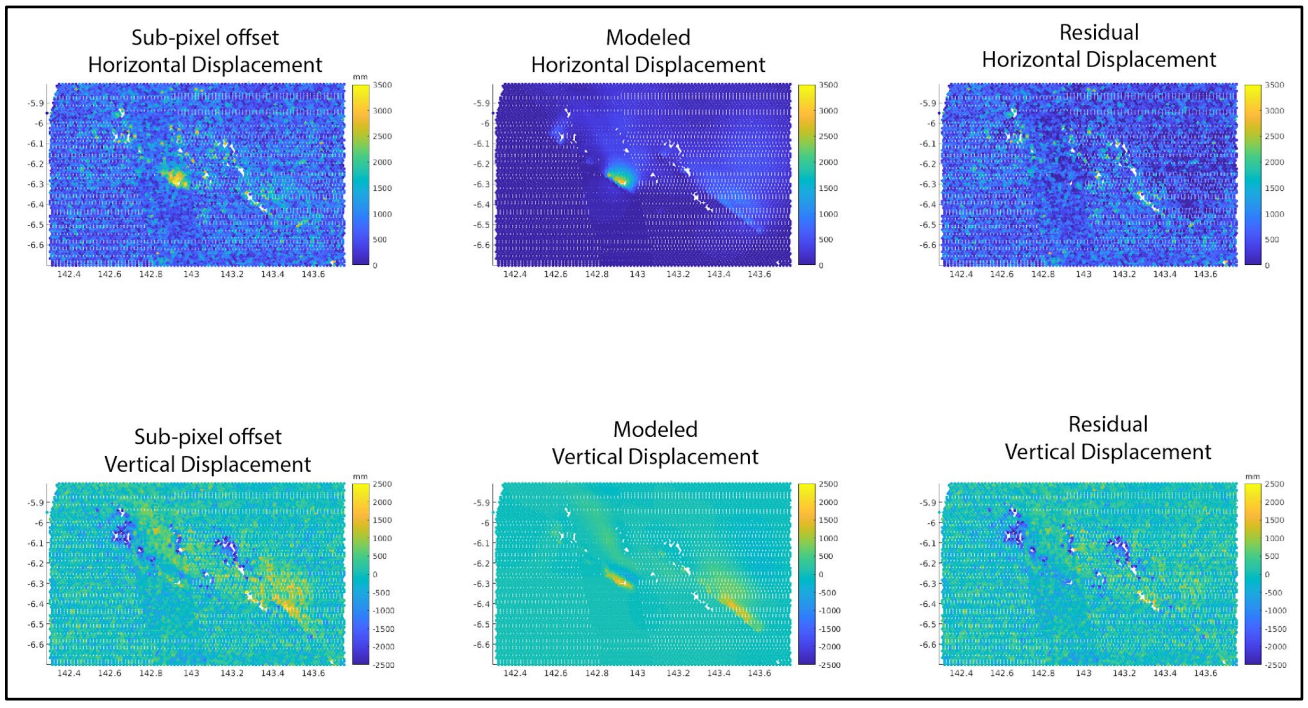

Figure A-3: Surface displacements of observed, modeled, and residual with landslide displacements without the fault boxes.

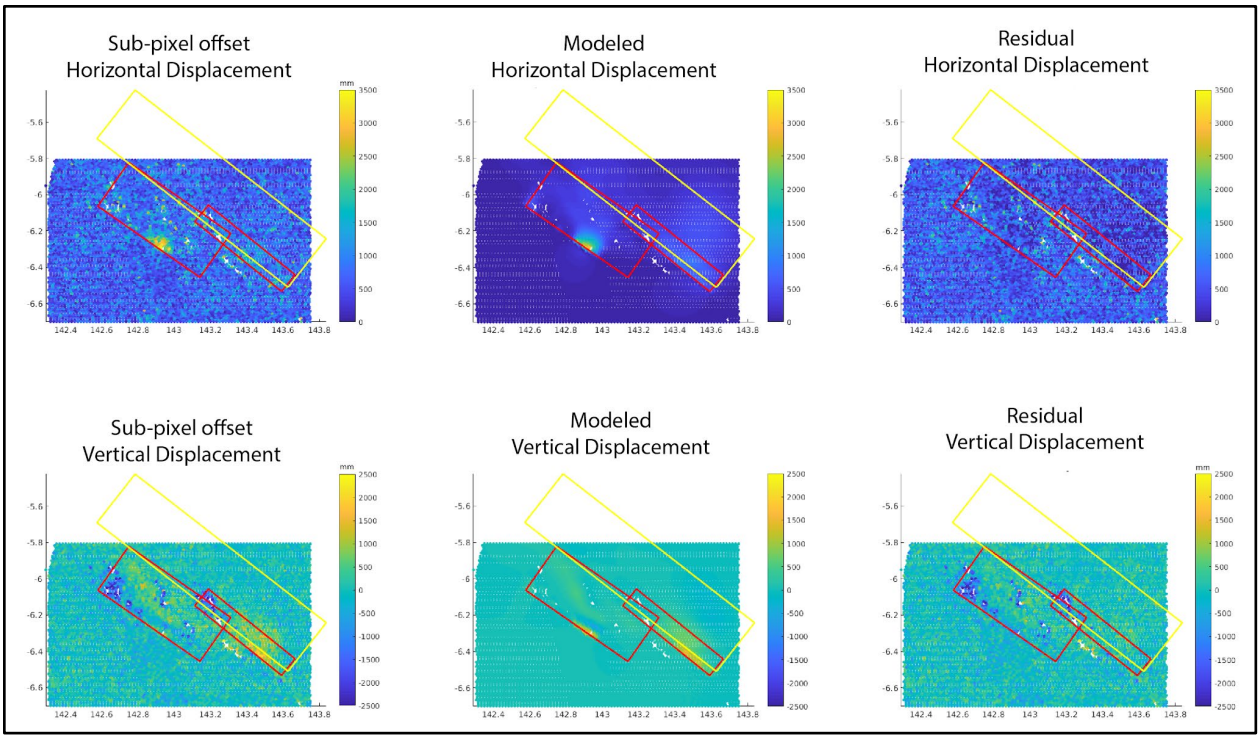

Figure A-4: Surface displacements without the removal of landslide displacements.

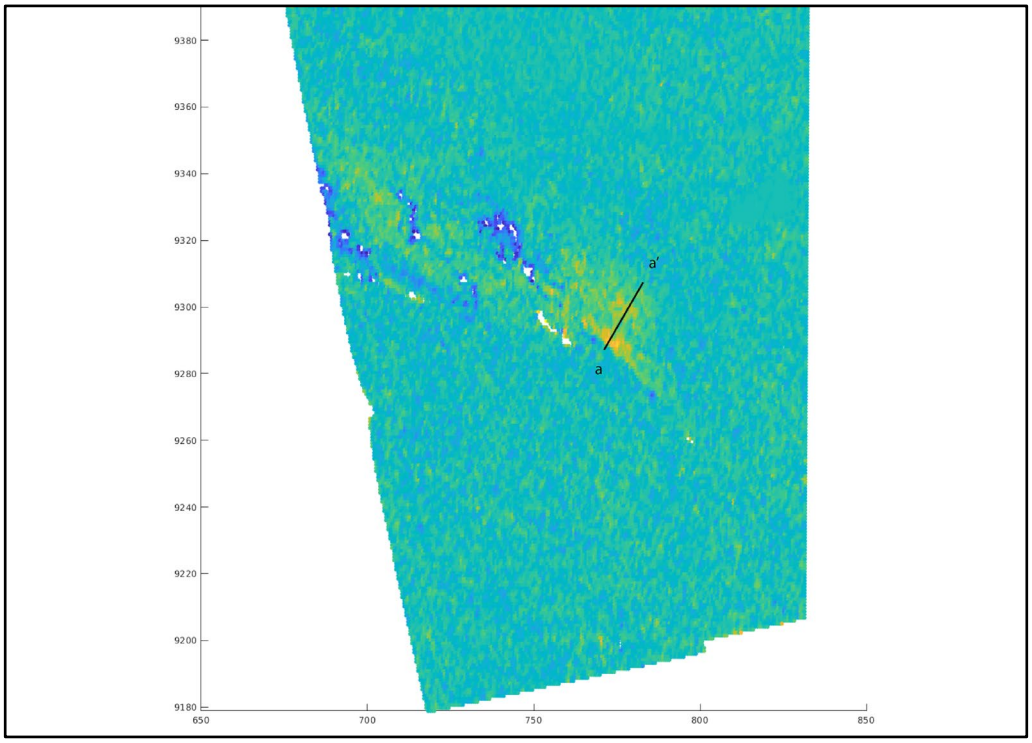

Figure A-5: Trace of surface displacement across the Mubi Fault. The x-axis is the UTM Easting in km and the Y-axis is the UTM Northing in km. The transect a-a' was used to indicate the cross-section of the surface displacement of the Mubi Fault.

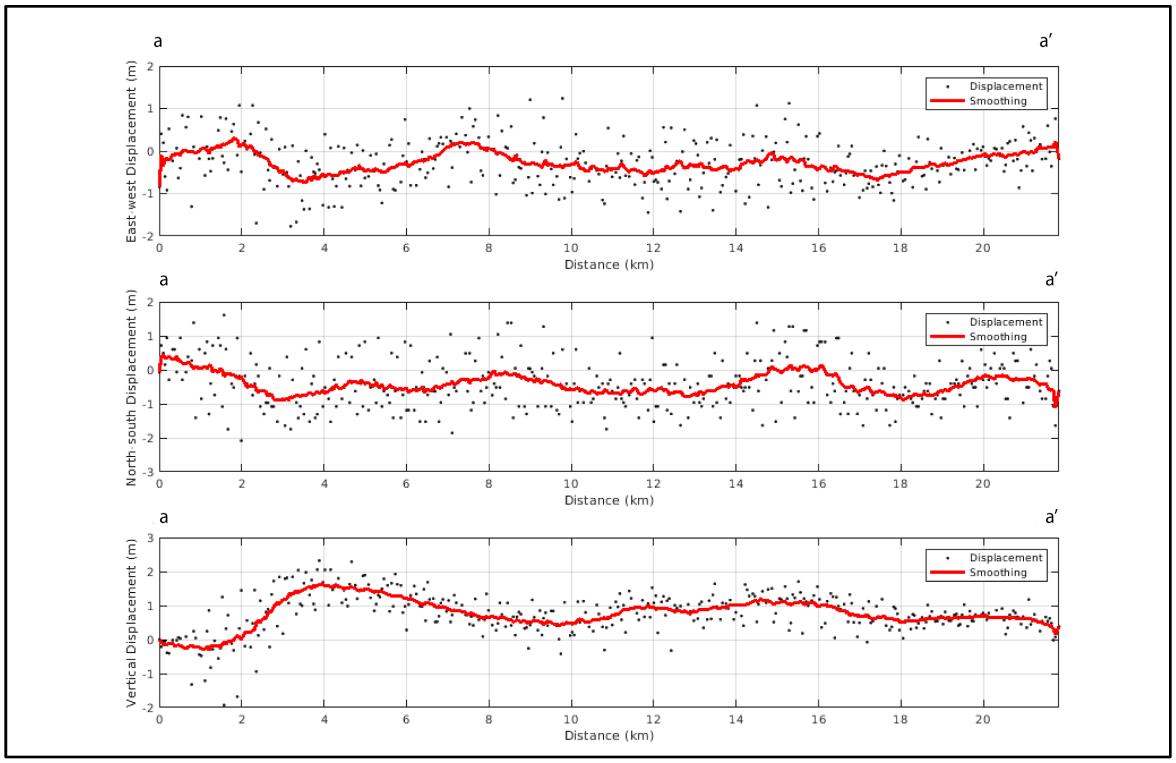

Figure A-6: Surface displacement across the Mubi Fault. SNR of 3 meters was used to generate these plots without the removal of landslides.

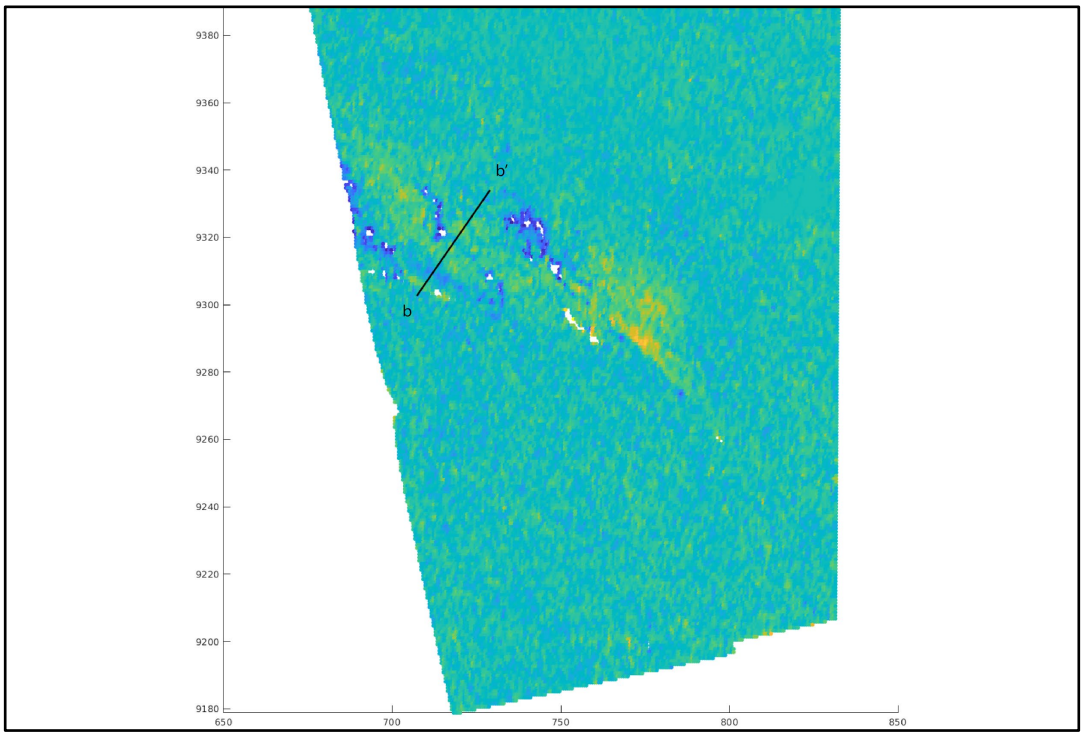

Figure A-7: Trace of surface displacement across the Mubi Fault. The x-axis is the UTM Easting in km and the Y-axis is the UTM Northing in km. The transect b-b' was used to indicate the cross-section of the surface displacement of the Mubi Fault.

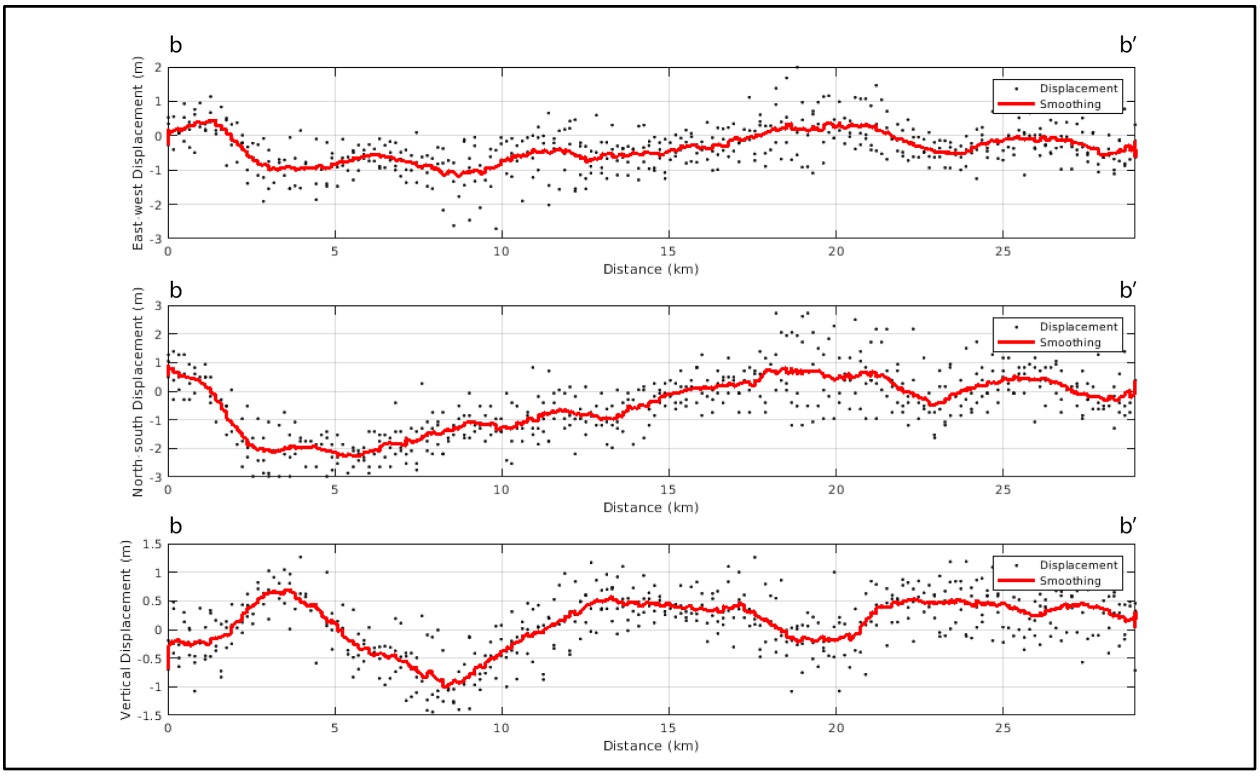

Figure A-8: Surface displacement across the Mananda Fault. SNR of 3 meters was used to generate these plots without the removal of landslides.

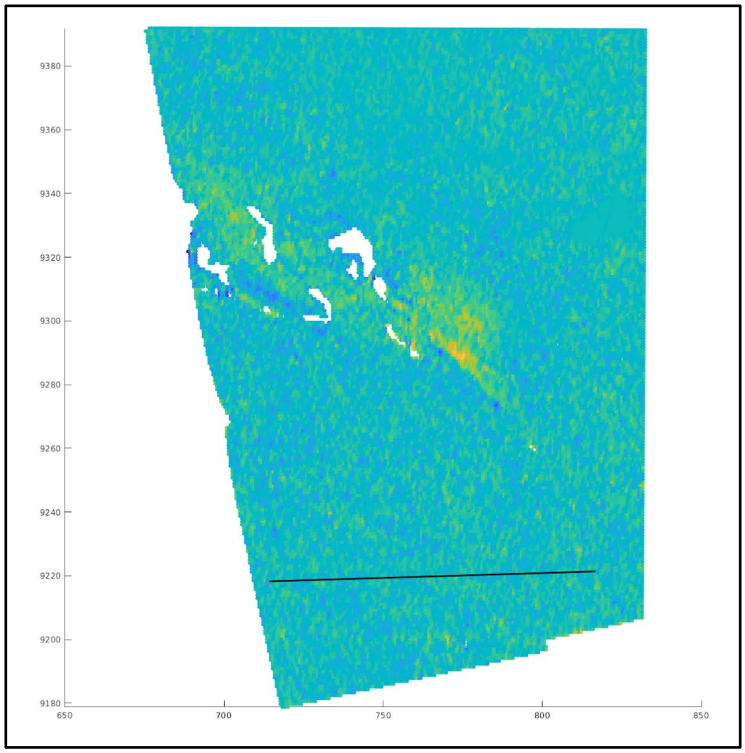

Figure A-9: Trace of the background surface displacement that was used to calculate the root-mean-square. X-axis and Y-axis are in UTM coordinates.

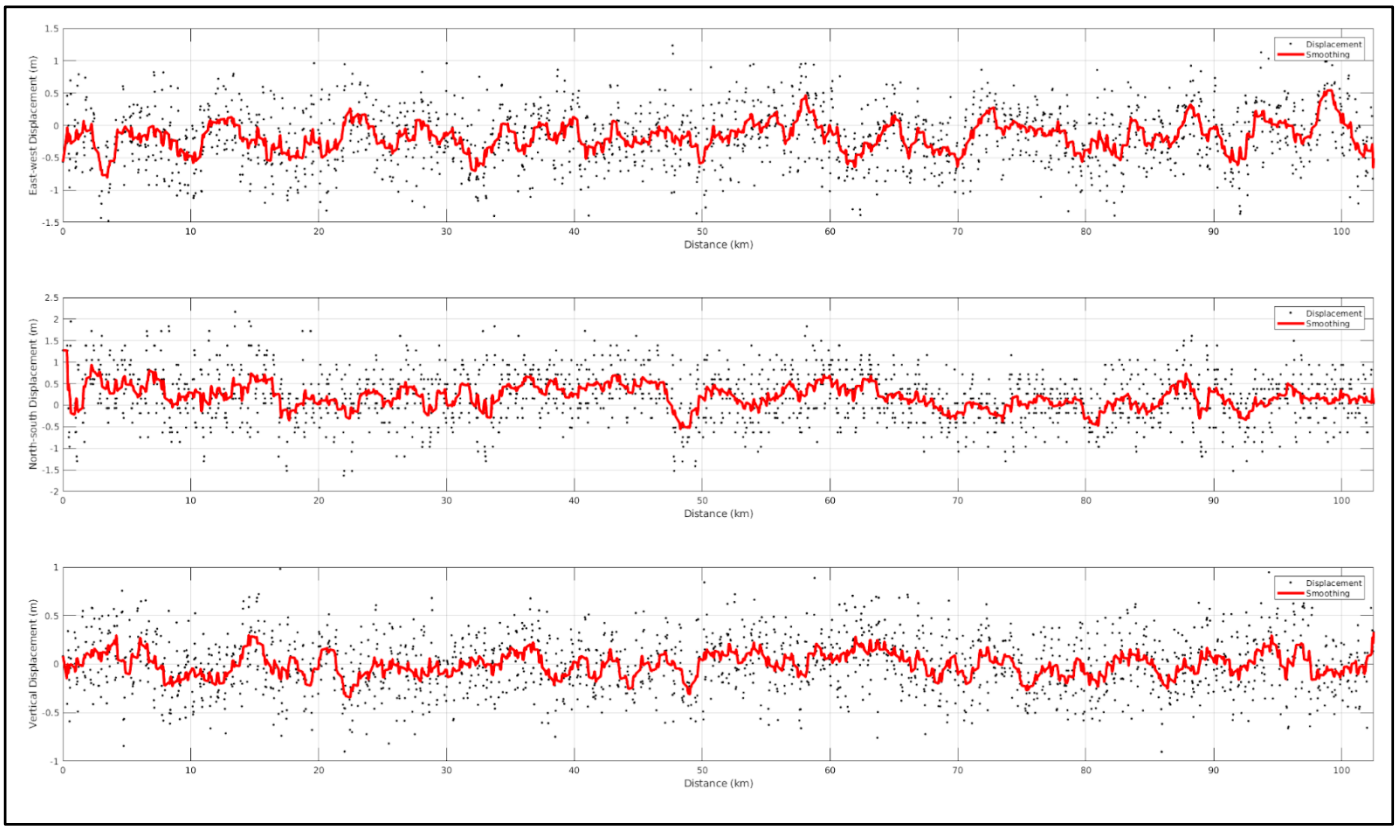

Figure A-10: The cross-section view of the root-mean-square of the background surface displacement.

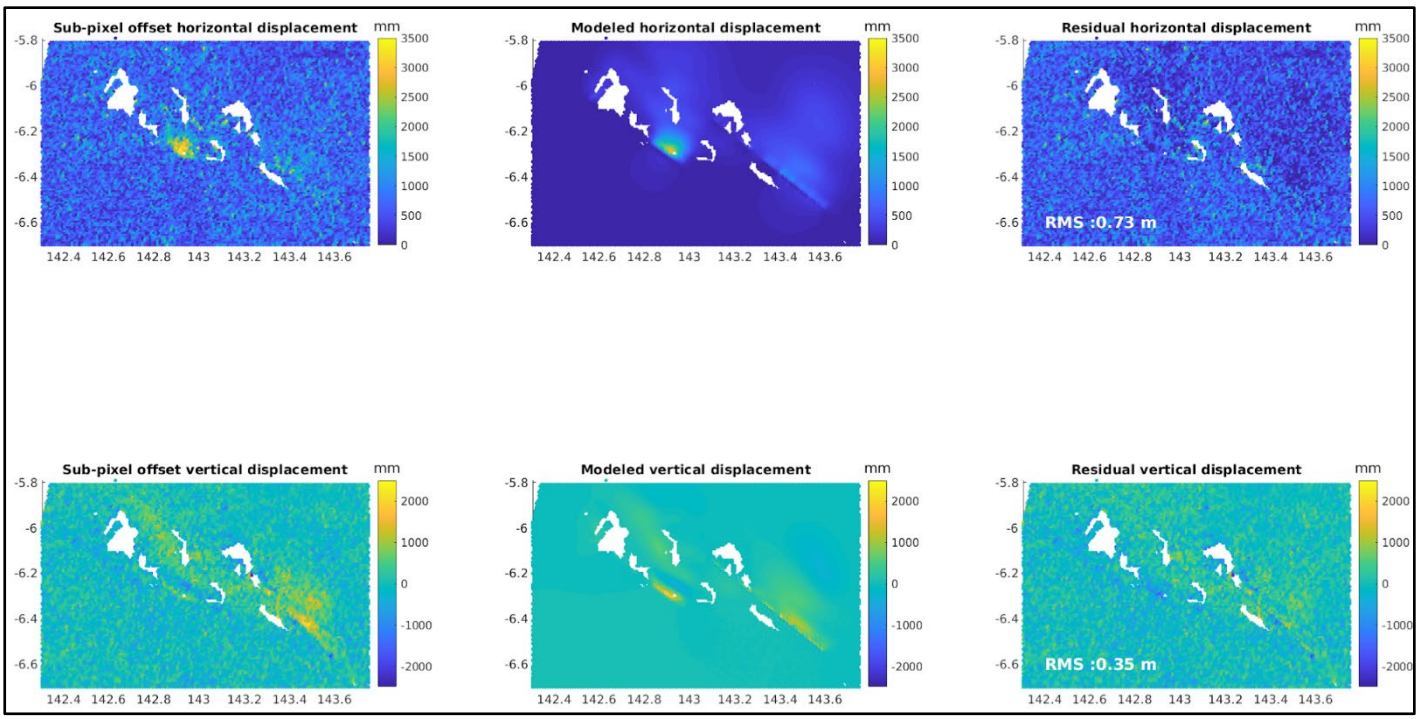

Figure A-11: Surface displacement without the landslides. Images on the top row is horizontal displacement and bottom row consist of vertical displacement. RMS is the misfit between the observed and modeled displacement.

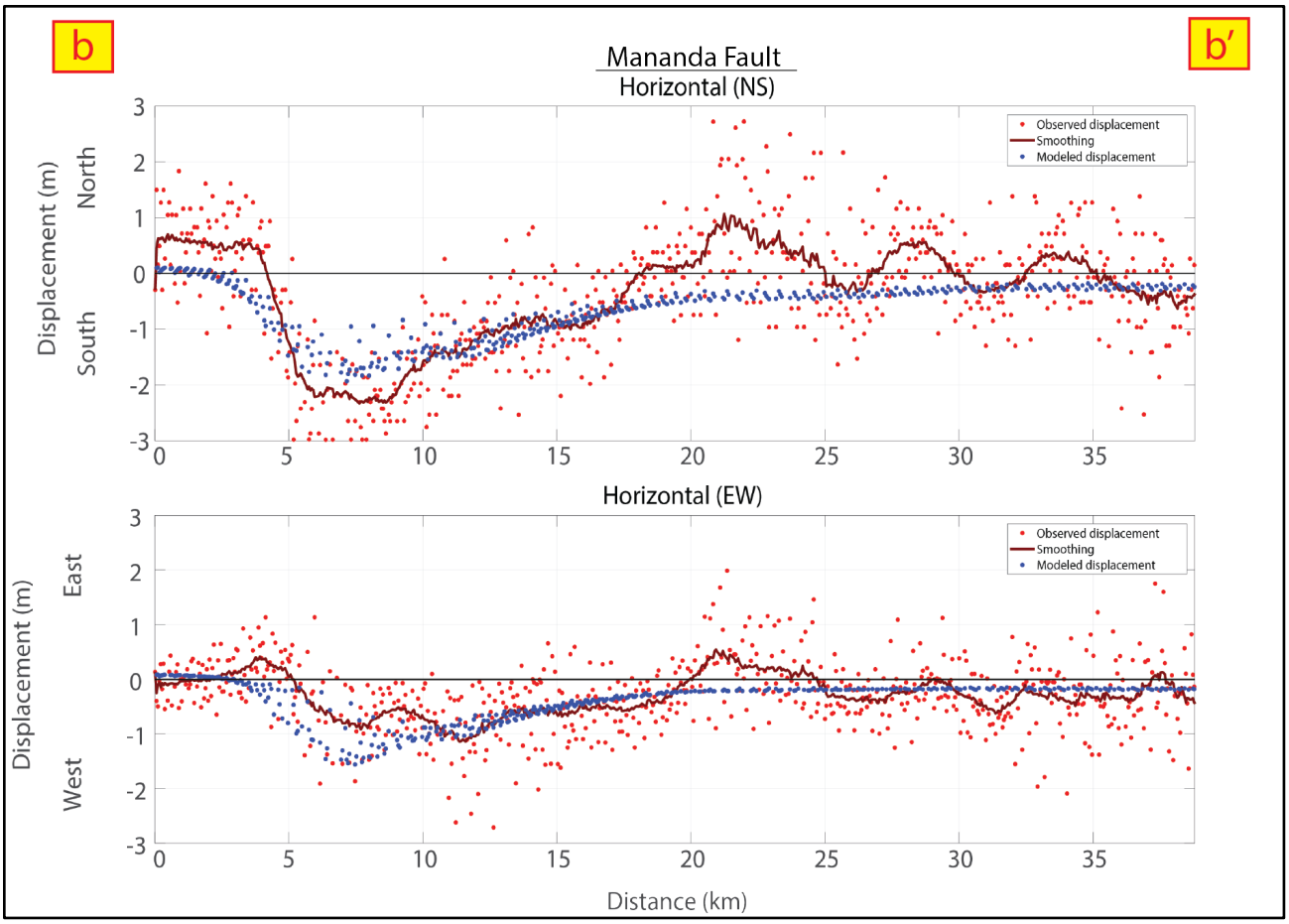

Figure A-12: Horizontal displacements with modeled displacement (in blue) across the Mananda Fault.

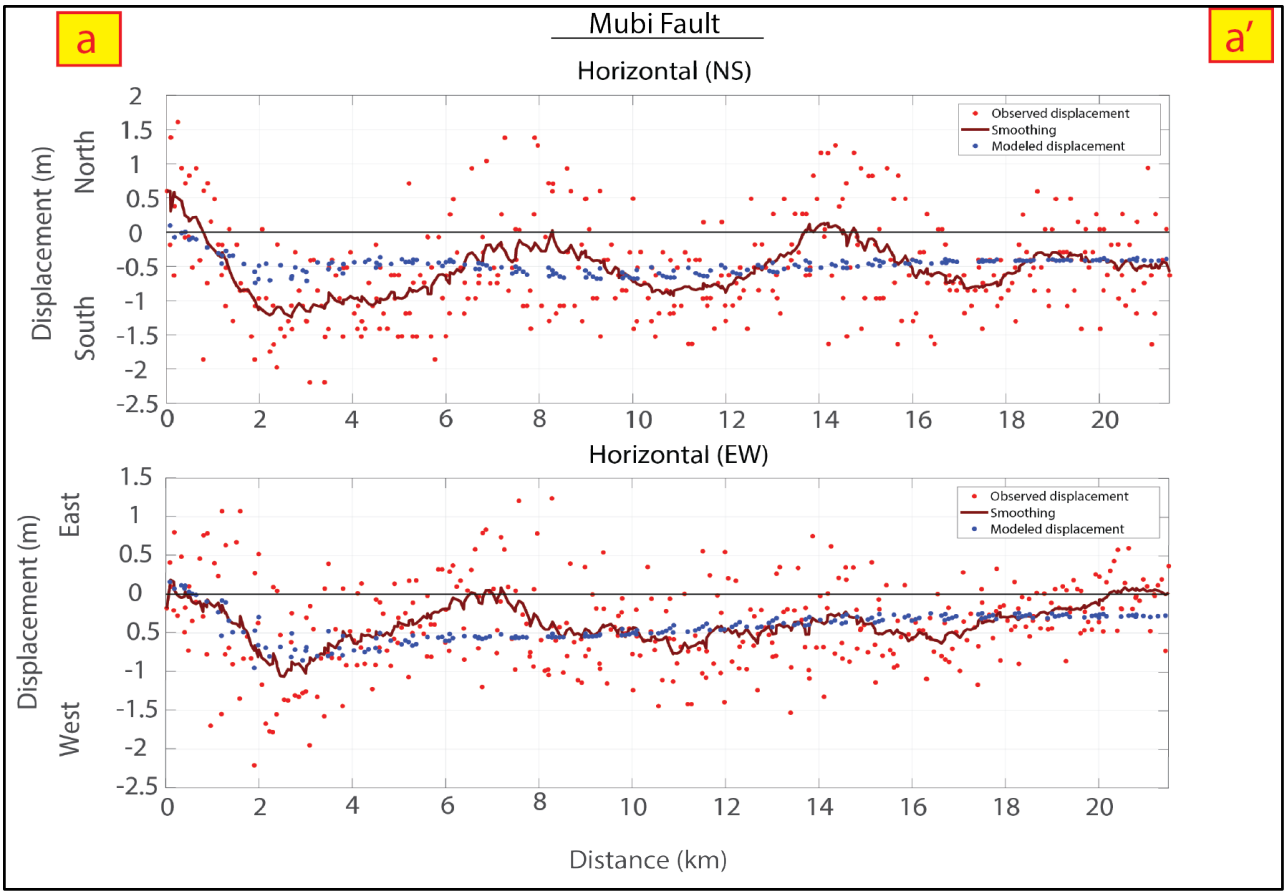

Figure A-13: Horizontal displacements (in red) with the modeled displacement (in blue) across the Mubi Fault.

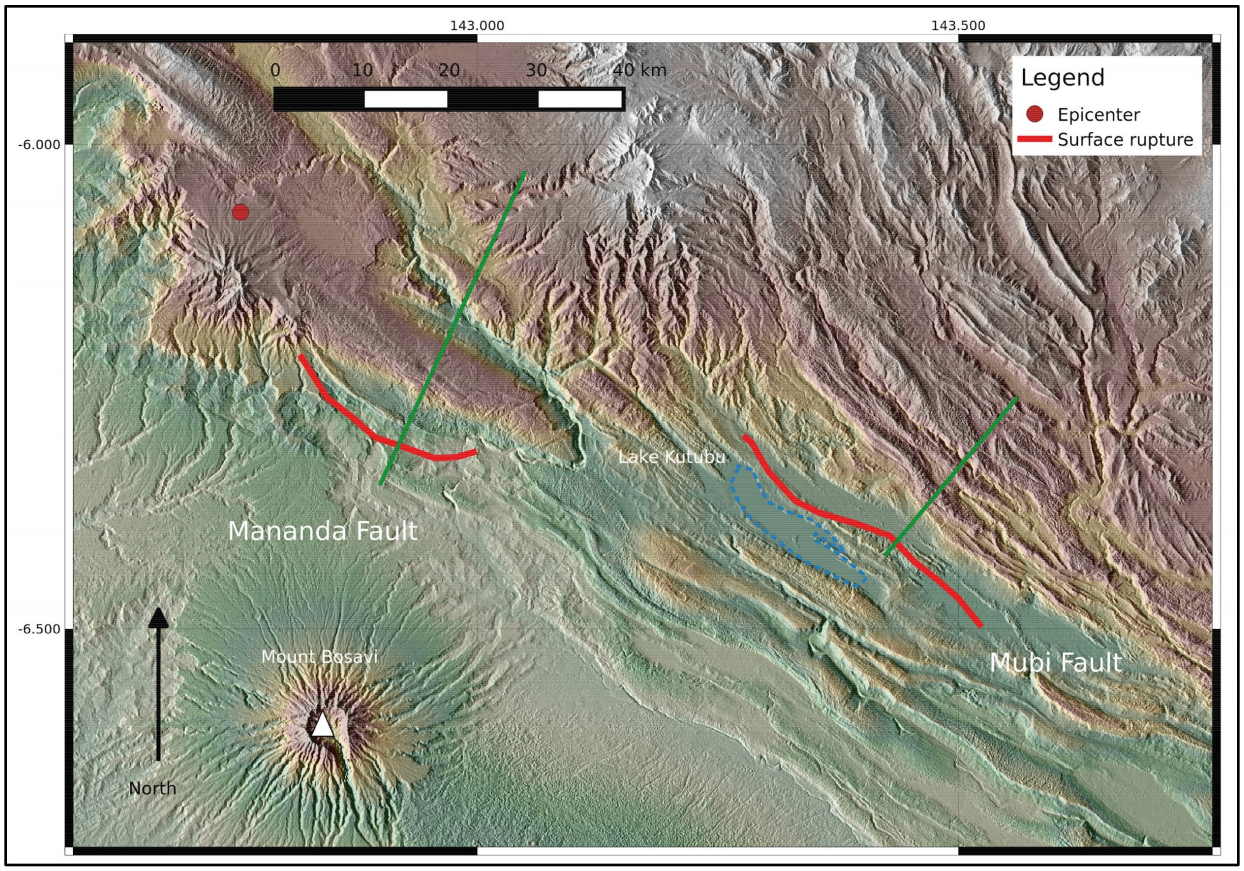

Figure A-14: Topographic map view of the Southern Highlands. The red dot represents the location of the mainshock on 25th February 2018. Green represents a lower elevation, closer to sea level and white indicates high elevation.

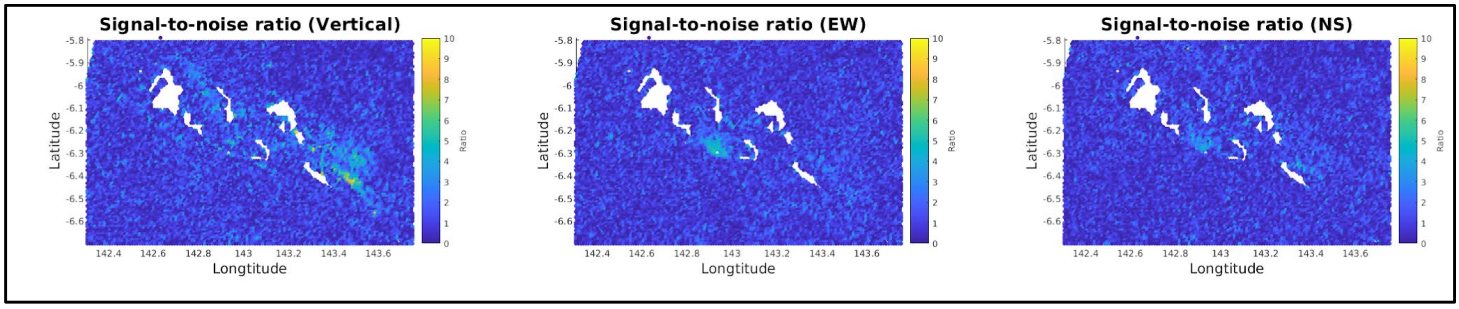

Figure A-15: Signal-to-noise ratio of the displacements without the landslides. A higher value indicates a higher signal-to-noise ratio.

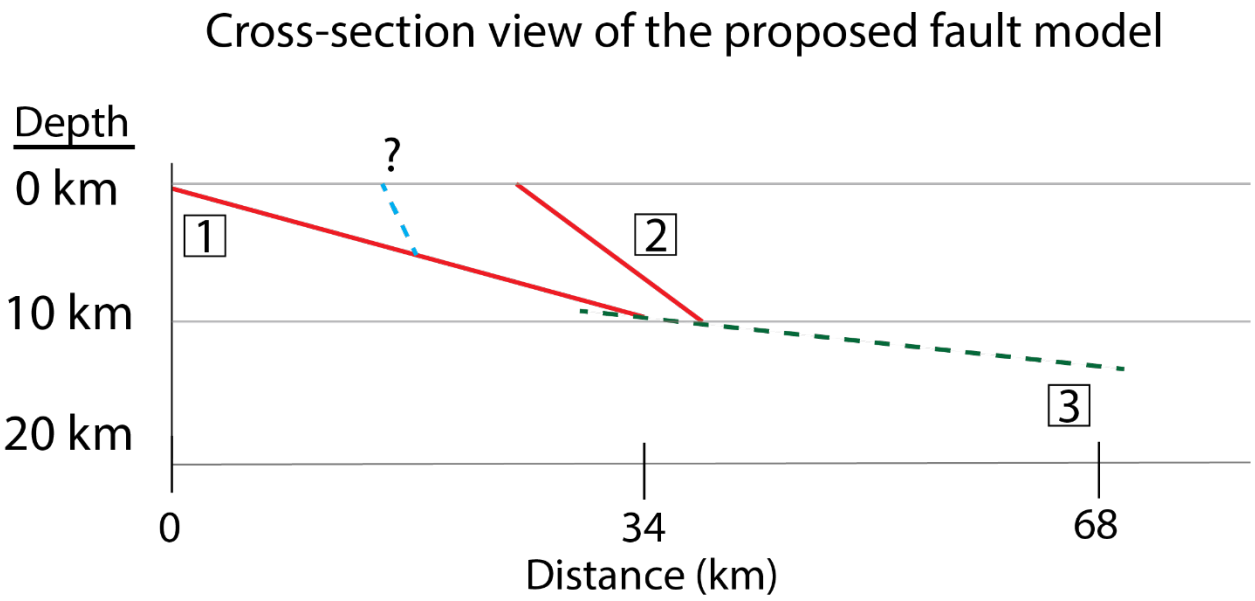

Figure A-16: Proposed fault model involving a smaller, steeper fault on Mubi Fault. Mananda Fault is labeled as 1, Mubi Fault is labeled as 2, and the detachment fault is labeled as 3.

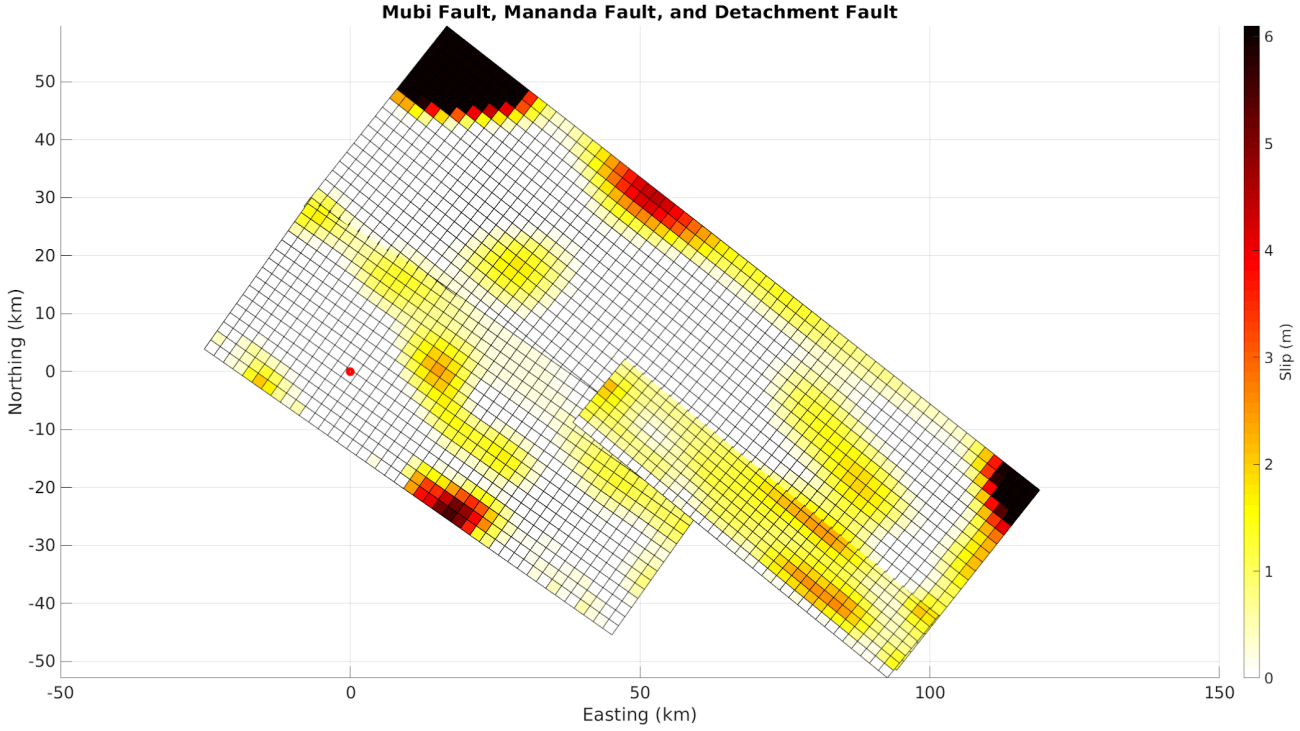

Figure A-17: Inverted fault model with the addition of Gaussian noise. Darker color indicates a higher amount of slip. White color indicates no slip.

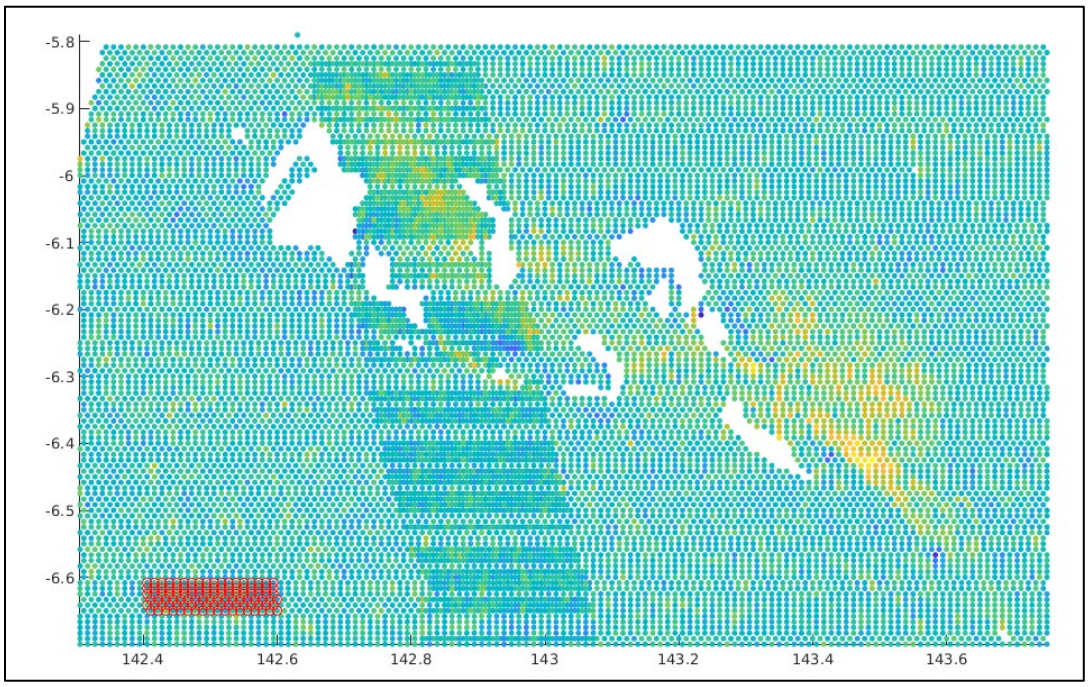

Figure A-18: Background noise area used to calculate root-mean-square. X-axis is the latitude and Y-axis is the longitude. The colors indicate the vertical displacement.

Supplement videos of the 3D fault slip models can be obtained via https://youtu.be/2IjZJIfdiqo